Understanding Induced Seismicity with a Discrete Fracture Network and Matrix Model with Mohr-Coulomb Failure and Nonlinear Hydraulic Diffusivity

D. T. Birdsell[1,2,3], H. Rajaram[1,4], and S. Karra[2]

[1]Department of Civil, Environmental, and Architectural Engineering, University of Colorado, Boulder, Colorado, USA
[2]Computational Earth Science Group, Earth and Environmental Sciences Division, Los Alamos National Laboratory, Los Alamos, New Mexico, USA
[3]Geothermal Energy and Geofluids Group, Department of Earth Sciences, ETH Zürich, Zürich, Switzerland
[4]Environmental Health and Engineering, Johns Hopkins University, Baltimore, Maryland, USA

Key Points:

- We introduce a discrete fracture network and matrix model with Mohr-Coulomb for induced seismicity
- Previous equivalent porous media models employed unrealistically-large hydraulic diffusivity values
- Fracture network density and sub-optimal fault orientation explain why seismicity is rare

Corresponding author: Daniel Birdsell, `danielbi@ethz.ch`

Abstract

Injection-induced seismicity (IIS) typically occurs when pressure diffuses from a sedimentary target formation down into fractured and faulted, low-permeability, critically-stressed basement rock. Previous studies of IIS have used basin-scale models of pressure diffusion that rely on an equivalent porous medium (EPM) approach to assign hydraulic diffusivity and a triggering pressure (TP) criteria for seismic initiation. We show that these models employed unrealistically-large values of hydraulic diffusivity, usually by neglecting the compressibility of the fractures in the specific storage coefficient, to result in pressure diffusion to seismogenic depths ($\geq$2 km into the basement). The EPM-TP approach does not explicitly represent the mechanical and hydrologic behavior of fractures and faults, and it fails to explain why relatively few disposal wells are associated with IIS. We develop a parallelized, partially-coupled, hydro-mechanical, discrete fracture network and matrix model (DFNM) model with thousands of fractures and the capability to calculate Mohr-Coulomb (MC) failure to indicate seismicity and alter hydraulic diffusivity. In consistent comparisons, DFNM-MC simulations allow for deeper, more heterogeneous pressure diffusion than EPM-TP simulations, and they do not need to employ unrealistic diffusivity values to result in pressure diffusion to seismogenic depths. A sensitivity analysis shows that small deviations in fault orientation ($\leq 2^{\circ}$ from optimal) and fracture network density outside an intermediate range can drastically decrease the likelihood of IIS, potentially explaining why only a small fraction of disposal wells are associated with IIS. The EPM-TP approach is unsuitable to investigate IIS, but the DFNM-MC approach offers a promising, nuanced approach for further study.

Plain Language Summary

Wastewater from the oil and gas industry is often injected into deep disposal wells far below groundwater aquifers. Injected fluids can migrate to deep faults via permeable fractures, where even small pressure changes can lead to human-caused earthquakes (HCEs). This suggests that most disposal wells should cause earthquakes, but only a small fraction actually do. Many previous studies of HCEs ignored fractures and faults, causing them to use unrealistic rock properties in their computer models, which led to misunderstandings about HCEs. We create a computer model that calculates how the fluid pressure moves rapidly through permeable fractures and causes earthquakes on faults. The results explain why HCEs only occur near a small fraction of disposal wells: first, fluid pressure can only reach a fault if the fractures form a connected hydraulic pathway to the fault, and second, even if fluid pressure reaches a fault, an earthquake only occurs for a narrow range of fault orientations. Scientists should stop using the old computer models that ignore fractures and faults to assess HCEs. To reduce HCEs, fluid should not be injected near: (a) permeable fracture networks with long-range connectivity, and (b) faults whose orientation is within the range that could produce earthquakes.

1 Introduction

Injection-induced seismicity (IIS) was first observed in Denver in the 1960s (Healy et al., 1968) and has become much more prevalent in the Central USA in the past decade (Ellsworth, 2013; Weingarten et al., 2015). In the USA, IIS can occur when wastewater, which is co-produced with oil and gas (O&G), is injected into disposal wells near basement rock. Since much of the crust is critically-stressed (Townend & Zoback, 2000), even slight perturbations in the pore pressure or stress state can lead to seismicity. Despite this fact, only a small fraction of wastewater disposal wells are spatio-temporally associated with IIS (Ellsworth, 2013; Nicholson & Wesson, 1992; Weingarten et al., 2015). The likelihood of IIS depends on the type of rock that underlies the disposal well, which is hypothesized to reflect the influence of fractures and faults that channel and focus fluid pressure in some rock types and not in others (Shah & Keller, 2017).

IIS is thought to occur when pore pressure diffuses down from the injection formation to underlying basement faults, thereby destabilizing them according to the Mohr-Coulomb (MC) shear failure criteria. The MC criteria depends on the in-situ stress state, the pore pressure, and the orientation and mechanical parameters of the fracture or fault (National Research Council, 2013). Most IIS occurs at depths $\geq$2 km below the top of the basement (BTB), which could be because the stress state and/or rheology of rock at that depth is more favorable for hosting earthquakes than shallower rock (Vilarrasa & Carrera, 2015). A hydraulic pathway composed of fractures and faults is required to bring elevated pressure to these seismogenic depths. The ability of these fractures and faults to act as a hydraulic pathway depends not only on their network topology, but also on the deformation of individual fractures and faults; increased pore pressure and shear failure (i.e. earthquakes) can dilate fractures and increase their permeability.

Much of the three-dimensional, reservoir- to basin-scale modeling efforts to understand IIS have relied on an equivalent porous media approach (EPM) to assign permeability and a triggering pressure (TP) approach for earthquake initiation. The EPM approach averages out the hydraulic effect of fractures, faults, and intact rock over large regions of the computational domain. The TP approach employs a single value of pressure increment, $\Delta P = TP$, to be associated with earthquake initiation. There are several important limitations to the EPM-TP approach. Firstly, the EPM-TP models have generally been used in an a posteriori sense, with the hydraulic diffusivity being calibrated to produce pressure at seismogenic depths. We suggest below that many of these studies employed unrealistically-large hydraulic diffusivity values, which calls their conclusions into question (see Sec. 2). Secondly, the EPM-TP models cannot explain why only localized regions of the basement exhibit IIS, even though they predict widespread continuous regions of elevated pressure in the basement. Thirdly, the EPM-TP approach cannot be used to forecast IIS because both the TP and the hydraulic diffusivity depend on properties of the fracture network, fault orientations, and geomechanics that the EPM-TP approach does not include.

In this paper we introduce a discrete fracture network and matrix (DFNM) model designed to understand how pore pressure diffuses through both matrix and fractures to seismogenic depths ($\geq$ 2 km BTB) in the context of IIS. It incorporates partial hydro-mechanical coupling, which allows alteration of hydraulic properties by normal and shear deformation of fractures, and calculation of MC failure. Although it is possible for shear failure to be aseismic in some cases (National Research Council, 2013), we assume that MC failure is an indicator of seismicity in this work. With its parallelization and simplifying mechanical assumptions, our model can simulate thousands of fractures and faults over large 3D domains, which is a step forward in the state of the art for modeling IIS at the reservoir to basin scale. It allows us to investigate some key research questions such as:

1. How exactly does fluid pressure diffuse through >2 km of fractured, low-permeability basement rock, and what is the effective hydraulic diffusivity of the *combined* fracture/matrix system?
2. How important are the deformation-induced changes on hydraulic diffusivity to the propagation of pressure?
3. Why are only a small percentage of disposal wells associated with IIS (Ellsworth, 2013; Nicholson & Wesson, 1992; Weingarten et al., 2015)? We would expect that the majority of disposal wells would be associated with IIS, since the entire crust is critically stressed (Townend & Zoback, 2000) and EPM-TP models show that pore pressure from deep disposal wells regularly diffuses to large regions of the basement (e.g. Keranen et al. (2014); Brown et al. (2017)).

Sec. 2 gives more background about wastewater disposal sites, previous approaches to modeling IIS, and the hydraulic diffusivity of fractured basement rock. Sec. 3 describes

our DFNM-MC approach. Sec. 4 describes our conceptual and numerical model of an IIS site that is inspired by Greeley, Colorado. Sec. 5.1 shows results that highlight the differences between the EPM-TP approach and the DFNM-MC approach, and Sec. 5.2 explores the importance of fracture intensity, fault orientation, and deformation-enhanced hydraulic diffusivity in a sensitivity analysis. Sec. 6 provides a discussion of our approach in context of other IIS modeling efforts, and the major conclusions.

2 Background

2.1 Description of Wastewater Disposal Sites

Information about disposal wells, geology of the target formation, and statistical observations of IIS are relatively abundant. US EPA Class II injection wells are permitted to inject waste fluids from O&G operations, and their regulations are focused on protecting underground sources of drinking water (i.e. relatively shallow, non-saline aquifers) (Zhang et al., 2013; Ellsworth, 2013). This means that wastewater disposal must take place in deep saline aquifers, which are usually thick, permeable, porous sedimentary rock, near basement rock. There are over 44,000 wastewater disposal wells in the U.S. (U.S. EPA, 2018), but only a small fraction of them are associated spatio-temporally with IIS (Ellsworth, 2013; Nicholson & Wesson, 1992; Weingarten et al., 2015). High-rate injection wells are more likely to be associated with IIS than low-rate injection wells (Weingarten et al., 2015), but there is also evidence that cumulative injection across many wells can cause IIS (Brown et al., 2017; Peterie et al., 2018; Langenbruch & Zoback, 2016). If the target formation sits atop a thick sedimentary unit or an extrusive rock, then IIS is less likely than if it sits atop fractured intrusive basement rock, which is hypothesized to be because flow is confined to fractures in intrusive rock, causing larger pressures (Shah & Keller, 2017). The importance of fractures in propagating pressure to seismogenic depths is a key feature that we explore in this paper.

Information about the crystalline basement rock, which hosts the majority of IIS hypocenters, is more difficult to find. Across Oklahoma, Colorado, and much of the Midwest, wastewater disposal often takes place in close proximity to crystalline basement rock (Shah & Keller, 2017; W. L. Yeck et al., 2016; Peterie et al., 2018; Zhang et al., 2013). Intact basement rock has very low in-situ hydraulic diffusivity, so fractures and faults are thought to act as the primary hydraulic pathways through the basement. The locations of large faults are sometimes already known from public maps and observations of previous seismicity, or can be mapped with gravity- and magnetic-based geophysical techniques (Shah & Keller, 2017), but the location of smaller basement faults and fractures are typically unknown or are proprietary data. Furthermore, many parameters that are relevant to understanding IIS (e.g. fracture orientation, mechanical properties, and hydrologic properties) are unknown for these fractures and faults. Nevertheless, it is possible to collect statistics of fracture properties, orientation, and density, which can be useful in modeling pressure diffusion (e.g. SKB (2011); Hyman et al. (2015)). Across Colorado, Oklahoma, New Mexico, and southern Kansas, most of the IIS is observed at least 2 km BTB and can be seen all the way to 8 km BTB (Nakai et al., 2017; W. L. Yeck et al., 2016; Schoenball & Ellsworth, 2017).

IIS occurs in the basement because it has a more favorable stress state and rheology to host seismicity than the shallower sedimentary rock. Most of the earth's crust is critically-stressed (Townend & Zoback, 2000), but the shallow, sedimentary rock tends not to be (Vilarrasa & Carrera, 2015). In fact, evidence from numerical modeling and frequency-depth distributions of natural earthquakes suggest that the crust may be most critically stressed at 5-6 km depth, which corresponds to $\geq$ 2 km BTB in many areas, depending on the thickness of sedimentary cover (Vilarrasa & Carrera, 2015). Furthermore, crystalline basement rock tends to deform in a brittle fashion, which encourages earthquakes, whereas sedimentary rock is softer and deforms in a more ductile fashion,

reducing the potential for earthquakes (Vilarrasa & Carrera, 2015). Finally, earthquakes tend to have larger magnitudes with greater depth, and there are concerns that density-driven flow due to brine injection will continue to diffuse pressure downward even as injection rates slow or stop (Pollyea et al., 2019), which further underscores the importance of understanding how pressure diffuses thorough basement rock to seismogenic depths.

While some studies have investigated how poroelastic stress changes or Coulomb static stress transfer can lead to induced seismicity (Goebel et al., 2017; Brown & Ge, 2018), the most prominent conceptual model of IIS posits that fluid pressure diffuses down into the basement faults, thereby destabilizing the faults and causing MC failure (Brown et al., 2017; National Research Council, 2013; Keranen et al., 2014; Langenbruch et al., 2018; Zhang et al., 2013; Nakai et al., 2017; Healy et al., 1968). There are at least two reasons why this pressure-diffusion conceptual model is popular. Firstly, increased pore pressure always destabilizes a fault, whereas poroelastic stress changes and Coulomb static stress transfer could act to destabilize *or* stabilize a fault, depending on the fault orientation and location. Secondly, poroelastic stress changes propagate very rapidly (at the speed of sound in rock), and therefore are inconsistent with the observation that there is usually a time lag between the beginning of injection and the onset of seismicity, suggesting a pore pressure diffusion process (Shapiro & Dinske, 2009). Since we are focused on the diffusion of pore pressure through kilometers of fractured, low-permeability, crystalline rock, we need to understand the hydraulic diffusivity of the combined fracture/matrix system, which is discussed in the next section.

2.2 Hydraulic Diffusivity

Hydraulic diffusivity is a rock property that describes how pore pressure diffuses through porous media. Based on the classical groundwater flow equation in porous media, which forms the basis for EPM models, the hydraulic diffusivity is defined as

$$c = \frac{K}{S_s} = \frac{k}{\mu(\phi\beta_w + \beta_m)} \tag{1}$$

where $K = k\rho g/\mu$ is the hydraulic conductivity, $S_s = \rho g(\phi\beta_w + \beta_m)$ is the specific storage, k is the permeability, ρ is the fluid density, g is gravity, μ is the dynamic viscosity of the fluid, ϕ is the porosity, β_w is the fluid compressibility, and β_m is the porous medium compressibility.

There are some subtleties in understanding and measuring hydraulic diffusivity in basement rock because it is composed of fractures and intact crystalline rock matrix. The permeability is dominated by fractures and faults, while the intact crystalline rock has very-low permeability. Faults can be either transmissive, sealing, or a combination thereof, and in this study we consider them as transmissive features. Furthermore, the hydraulic diffusivity of fractures is also a function of geomechanical deformation. Fractures that are held open, for example by high pore pressures, are more permeable and store more fluid than closed fractures. The permeability of the combined fracture/matrix rock decreases with depth (Manning & Ingebritsen, 1999), and one of the contributing factors could be the increased lithostatic stress that forces fractures closed. Shear dilation after MC failure can also alter the permeability and fluid storage within a fracture.

Hydraulic diffusivity depends on the scale over which it is measured (Townend & Zoback, 2000). At the core scale, permeability of crystalline rock can vary from 10^{-24}–10^{-17} m^2, and it decreases with depth and confining pressure (Freeze & Cherry, 1979; Morrow & Lockner, 1997). The compressibility of unfractured granite is $\sim 10^{-11}$ Pa^{-1} (De Marsily, 1986), and porosity is $\leq$0.05 (Freeze & Cherry, 1979). Using these parameters, the hydraulic diffusivity for an unfractured granite at the core scale is $10^{-10} \leq c_{core} \leq 10^{-4}$ m^2/s. At the reservoir scales over which IIS is observed (1 – 10 km), estimates of c are larger. The bulk compressibility of jointed rock ranges from 10^{-10} – 10^{-8} Pa^{-1} (Freeze & Cherry, 1979). The bulk permeability of fractured basement rock de-

pends on the fracture network, but has been estimated to be 10^{-17} – 10^{-16} m^2 (Townend & Zoback, 2000). Using these parameters, the hydraulic diffusivity for bulk, fractured, reservoir-scale rock is expected to range between $10^{-6} \leq c_{bulk} \leq 10^{-3}$ m^2/s.

Hydraulic diffusivity has also been estimated based on space-time patterns of seismic clouds following injection or reservoir impoundment. Talwani et al. (2007) used this approach to infer an apparent "seismogenic diffusivity" in the range $0.1 < c_{sT} < 10.0$ m^2/s. We use the notation c_{sT} to denote seismogenic diffusivity in the sense of Talwani. However, it is unclear whether the seismogenic diffusivity is the same as the hydraulic diffusivity. Shapiro and Dinske (2009) interpret estimates of c following an EPM interpretation, but the EPM hydraulic diffusivity derived from a seismic cloud can be an overestimation of the actual EPM hydraulic diffusivity, when permeable fractures are embedded within a low-permeability matrix (Haagenson et al., 2018a, 2018b). Talwani et al. (2007) interpret c_{sT} as the hydraulic diffusivity associated with induced seismicity, assuming single linear fractures connect the fluid source with the hypocentral location. The hydraulic diffusivity of a parallel-plate fracture using the cubic law for permeability can be approximated as (Murphy et al., 2004):

$$c = \frac{b^2}{12\mu(\beta_w + \beta_f)} \tag{2}$$

where b is the hydraulic aperture, $\beta_f = b^{-1}(db/d\sigma_n^{'})$ is the fracture compressibility, and $\sigma_n^{'}$ is the effective normal stress. However Talwani et al.'s analysis neglect leakoff from fractures and tortuosity of fracture flow paths, both of which lead to slower pressure diffusion. Therefore, we expect that the inferred c_{sT} values are smaller than the true hydraulic diffusivity of the fractures. Table 1 shows the values of basement hydraulic diffusivity at the core and reservoir scale, the seismogenic diffusivity, and the values of hydraulic diffusivity employed by several EPM-TP modeling studies. These values are important to keep in mind when considering conceptual and numerical models of pore pressure diffusion in the context of IIS.

2.3 Previous Approaches to Modeling Pressure Diffusion That Causes IIS

In general, models of IIS should couple the equations of pressure diffusion and geomechanics (i.e. employ a hydro-mechanical approach) for a rock mass containing discontinuities in the form of fractures and faults. However, hydro-mechanical equations are challenging to solve on scales of the order of tens of kilometers even assuming the rock mass behaves as a continuum. Proper treatment of discontinuous displacements across fractures and faults makes the problem even more challenging. Although fully coupled hydro-mechanical models have been presented, which qualitatively reproduce the phenomenology of IIS, they have largely been demonstrated either without explicit consideration of fractures and faults (e.g. Shirzaei et al. (2016)) or in limited 2D domains (e.g. Jin and Zoback (2017, 2018)).

Most large-scale modeling studies of IIS are based on the groundwater flow equation, simulate pressure diffusion from an injection well, and assume that seismicity is associated with exceedance of a critical threshold pressure, which we refer to as TP. These EPM-TP models typically neglect the large disparity in permeability between connected fractures and the surrounding low-permeability basement rock, and assume a homogeneous EPM. These models have been employed a-posteriori to demonstrate TP at locations of IIS in several studies (Keranen et al., 2014; Brown et al., 2017; Nakai et al., 2017; Shirzaei et al., 2016). However, most of these studies assume unrealistically-large values of hydraulic diffusivity, in order to achieve rapid pressure diffusion to the location of seismicity (see Table 1). EPM-TP models also are unable to explain why IIS does not occur at all sites where the pressure exceeds TP. In the subsections below, we describe the EPM-TP models and fully-coupled hydro-mechanical models that include flow

Table 1. The crystalline-basement rock hydraulic diffusivity observed experimentally and used in several modeling studies. The first three table entries are experimental- or field-determined values for different length scales and techniques. The next five entries show the hydraulic diffusivity employed in EPM modeling studies, which are larger than c_{bulk}. The next five entries show studies that use an EPM model with a permeable fault. They generally employ smaller c for the intact basement, but in most cases it is still larger than c_{bulk}. The final two entries show the hydraulic diffusivity used in our comparison between a DFNM model and a corresponding EPM model with permeability assigned from a numerical permeameter test on the DFNM (see Sec. 4.4 and 5.1).

Experiment or Study	Basement Rock c (m^2/s)	Fracture or Fault c (m^2/s)
Unfractured granite at core scale (c_{core})	10^{-10} – 10^{-4}	N/A
Fractured granite at reservoir scale (c_{bulk})	10^{-6} – 10^{-3}	N/A
Seismogenic fractures (c_{sT})	N/A	10^{-1} – 10^{1}
Brown et al. (2017)[a]	10^{-3} – $4 \cdot 10^{0}$	N/A
Keranen et al. (2014)	10^{-2} – 10^{-1}	N/A
Langenbruch et al. (2018)[d]	$2 \cdot 10^{-1}$	N/A
Pollyea et al. (2019)[b]	10^{-3} – 10^{-1}	N/A
Shirzaei et al. (2016)[a]	10^{-2} – 10^{-1}	N/A
Nakai et al. (2017)[a,d]	10^{-4} – 10^{-2}	10^{-1}
Hearn et al. (2018)	10^{-7}	$3 \cdot 10^{0}$ – $3 \cdot 10^{1}$
Zhang et al. (2013)	$2 \cdot 10^{-3}$	10^{1}
Ogwari et al. (2018)[d]	10^{-7}	10^{-2} – 10^{-1}
Schoenball et al. (2018)[c]	Not Reported	Not Reported
DFNM model (Sec. 5.1)	10^{-5}	$\sim 5 \cdot 10^{3}$
Scenario EPM1 (Sec. 5.1)	$\sim 2 \cdot 10^{-4}$	N/A

[a]Basement hydraulic diffusivity decreases with depth.
[b]Dual continua model, c calculated from reported volume-weighted k and ϕ.
[c]Compressibility is not reported, so hydraulic diffusivity cannot be calculated.
[d]Hydraulic diffusivity is calculated with assumed fluid properties: $\rho = 1000$ kg/m^3 and $\mu = 0.001$ Pa-s.

in discrete fracture(s) or fault(s). Tables S1 and S2 summarize the physics of the models that are discussed in this section.

2.3.1 EPM-TP and Similar Models

EPM models have generally employed unrealistically large (often by a few orders of magnitude) values of hydraulic diffusivity to propagate pressure to seismogenic locations. For EPM models, c should equal c_{bulk}, but all of the EPM studies (Keranen et al., 2014; Brown et al., 2017; Langenbruch et al., 2018; Shirzaei et al., 2016; Pollyea et al., 2019) have used significantly larger values (see Table 1). For models that include one or two faults (Nakai et al., 2017; Hearn et al., 2018; Zhang et al., 2013; Ogwari et al., 2018; Schoenball et al., 2018), it could be argued that c in the unfaulted part should be assigned to c_{bulk} (if one assumes that the basement away from the fault is highly fractured), or to c_{core} (if one assumes that the unfaulted basement is minimally fractured). But many of these studies employ values of c in the unfaulted basement that are larger than, or at the upper end of the range for c_{bulk} and c_{core}. In many cases, the problem in the employed value of c comes from the assignment of the specific storage ($S_s < 10^{-6}$ m^{-1}) or, equivalently, the compressibility ($\beta_m < 10^{-10}$ Pa-1), both of which ignore the compressibility of basement fractures and inflate the value of c (see Eq. 1) (e.g. Brown et al. (2017); Langenbruch et al. (2018); Nakai et al. (2017); Pollyea et al. (2019)). Not only do the EPM models employ incorrect values of c, some follow logic that leads to questionable conclusions. For example, they calibrate c to encourage pressure increment $> TP$ at locations of observed seismic clouds, and then they conclude that pressure diffusion is a plausible causative mechanism of seismicity (Keranen et al., 2014; Brown et al., 2017)). We show in Sec. 5.1 that an EPM model with realistic values of c would actually show the opposite - that pressure diffusion is not a plausible mechanism of earthquake triggering. Only fracture-based models seem to be able to explain pressure propagation to seismogenic depths, and only in small, localized regions of the basement (Sec. 5).

Another problem with the EPM-TP approach is that it cannot explain why earthquakes *do not* occur at some locations. The EPM approach results in very smooth pressure profiles, which are probably unrealistic given the heterogeneity that fractures and faults introduce, wherein $\Delta P > TP$ in regions of the basement that are much larger than the seismic regions (e.g. Brown et al. (2017) Fig. 4d). There are several reasons why seismicity may not occur in these regions: (a) pressure has not actually diffused there, (b) there are no favorably-oriented faults there, or (c) the stress state is less critical, but the EPM-TP cannot evaluate which may be the case. This is illustrated in Fig. 4D of Keranen et al. (2014), where the average pressure upon failure is 0.07 MPa, but ranges from 0.04 to >0.4 MPa. We show in Sec. 5.2 that very small variations in fault orientation and triggering pressure (as low as 2° and 0.13 MPa, respectively) can drastically reduce the likelihood of an earthquake. Finally, we note that some of the studies cited in this section may incorporate more advanced triggering mechanisms (Zhang et al., 2013; Schoenball et al., 2018), mechanical coupling (Shirzaei et al., 2016), a hybrid physical-statistical model (Langenbruch et al., 2018), or a dual continua approximation (Pollyea et al., 2019) (see Table S1), but they are still EPM-TP models or have similar drawbacks to the EPM-TP models.

2.3.2 Hydro-Mechanical, MC, Fracture and Matrix Models

There is another class of models that includes much more of the relevant physics for understanding IIS. These models solve the fully-coupled hydro-mechanical equations, include fracture(s)/fault(s), calculate Mohr-Coulomb failure, and account for the changes in hydraulic properties due to mechanical deformations (Jin & Zoback, 2018, 2017; Jha & Juanes, 2014; Ucar et al., 2018; Rinaldi et al., 2014; Kelkar et al., 2014; Chang & Segall, 2016). Many of these studies also account for even more advanced earthquake physics such as strain-softening (Rinaldi et al., 2014; Jha & Juanes, 2014), or multiple failure

events on a given fracture (Jin & Zoback, 2018). They would be ideal tools to investigate pressure diffusion related to IIS, but they are computationally expensive and therefore limited to small spatial scales, limited number of fractures/faults, and/or 2D domains. Furthermore, these models have not been used to investigate how pressure propagates from a disposal well into the deep basement ($>$ 2 km BTB), either because they focus on geothermal energy (Ucar et al., 2018; Kelkar et al., 2014) and carbon sequestration (Rinaldi et al., 2014; Jha & Juanes, 2014), or because the simulation is focused on pressure diffusion near the wellbore, rather than to seismogenic depths (Jin & Zoback, 2018, 2017; Chang & Segall, 2016). There are other studies that do not fall neatly into the EPM/TP category of Sec. 2.3.1 or the hydro-mechanical, MC, fracture models of this section. Some models use a rate-and-state seismicity model, as an alternative to the MC criteria, and couple to pressure diffusion models to predict the rise and fall of seismicity rates (Dempsey & Riffault, 2019; Riffault et al., 2018; Norbeck & Rubinstein, 2018). Others perform a partial hydro-mechanical coupling and calculate MC failure on seed points that represent potential earthquake hypocenters (Rinaldi & Nespoli, 2017).

3 DFNM-MC Modeling Approach

Our goal is to present a modeling approach that improves significantly upon the EPM-TP approach, while facilitating computational tractability for 3D simulations on scales of the order of tens of km with thousands of fractures and faults. We follow the approach of previous hydro-mechanical, MC, fracture-matrix models (see Sec. 2.3.2), but we introduce some simplifying assumptions to decrease computational cost. The salient features of our approach are:

1. Discrete fractures and faults are explicitly represented, and their properties are assigned in a physically consistent manner. Fracture orientations are variable. Fluid flow in both the fracture and rock matrix are represented.
2. The rock matrix properties are consistently within accepted ranges for properties of basement rock.
3. The model allows rapid pressure diffusion along connected fractures without resorting to unrealistically low values for medium compressibility.
4. A partially coupled approach, wherein the fracture hydraulic diffusivity is allowed to evolve as a function of effective normal stress on a fracture plane, and in response to slip events. The approach is only partially coupled because the initial stress state is specified and is assumed to be time-invariant. However, the time variation of effective stress due to pressure diffusion is captured in this approach.
5. Although rapid pressure diffusion through a connected network of fractures occurs, seismic events occur only when the MC failure criterion is satisfied along a fracture or a fault. Thus, failure events only occur along favorably oriented fractures/faults. The model can thus provide an explanation for why IIS occurs only at a small fraction of deep wastewater injection sites.

We call this the discrete fracture network and matrix with Mohr Coulomb failure (DFNM-MC) approach – it allows for flow in a discrete fracture network (DFN) and the surrounding rock matrix. The pressure at which MC failure occurs on a fracture of fault depends on its orientation and the local stress state. The most favorable orientation corresponding to the minimum pressure is determined by the initial stress state.

Within this DFNM-MC framework, there is no distinction between a fracture and a fault other than the size of the feature. This DFNM-MC approach has been validated against analytical and numerical solutions in previous work (Birdsell, Rajaram, & Karra, 2018; Birdsell, 2018). In Sec. 3.1 we discuss and justify the partially-coupled hydro-mechanical approach, which allows us to simulate important mechanical processes without resorting to the higher complexity and computational cost of a fully-coupled hydro-mechanical

approach. In Sec. 3.2, we describe the equations of flow in porous media and in fractures/faults and we show how the constitutive relationships for porosity and permeability can be altered in fractured grid cells so that the simulator can consistently solve for both fracture and matrix flow in a single domain. In Sec. 3.3, we describe how the hydraulic diffusivity is treated as a function of normal and shear deformation.

3.1 Framework of Partially-Coupled Hydro-Mechanical Approach

Our numerical model is focused primarily on pore pressure diffusion, but it is partially coupled to geomechanics to capture some of the physics that are relevant to IIS. The aspects of IIS that require geomechanical coupling include: (a) evaluation of the MC failure criteria, and (b) the influence of mechanical deformations on the hydraulic diffusivity of fractures. We assume that the in-situ stress state is a function of space but is frozen in time. This may seem like an oversimplification, but it captures many of the physical complexities that the EPM-TP approach does not. For example, fractures that are subject to a large compressive normal stress are forced closed and therefore less permeable; such behavior is readily captured within the framework of the partially coupled approach. Furthermore, MC failure criteria depends on fracture orientation, which is also explicitly represented in a DFNM framework. This partially-coupled approach dramatically reduces computational expense in comparison to fully coupled approaches, while still honoring fundamental aspects of geomechanics as they relate to IIS.

The normal stress on a fracture/fault is calculated as $\sigma_n(\boldsymbol{x}) = (\boldsymbol{\sigma}(\boldsymbol{x})\boldsymbol{n})\cdot\boldsymbol{n}$ where $\boldsymbol{\sigma}(\boldsymbol{x})$ is the second-order stress tensor as a function of the position vector, $\boldsymbol{x}$, describing the location in the domain, and $\boldsymbol{n}$ is the unit vector normal to the fracture plane. The magnitude of the shear stress is calculated as $|\boldsymbol{\tau}| = |(\boldsymbol{\sigma}(\boldsymbol{x})\boldsymbol{n}) \times \boldsymbol{n}|$. The code is capable of resolving the entire stress tensor $\boldsymbol{\sigma}$, but we assume that the principal components of stress are vertical and horizontal in all of the simulations presented in this paper, which is representative for much of the subsurface (Zoback, 2010), and we use the principal coordinate system so that there are no shear stresses in the stress tensor. The vertical stress, the maximum principal horizontal stress, and the minimum principal horizontal stress are denoted by σ_v, $\sigma_{H,max}$, and $\sigma_{h,min}$, respectively. We assume that the horizontal stresses take the following form: $\sigma_{H,max} = \alpha_1\sigma_v$, and $\sigma_{h,min} = \alpha_2\sigma_v$ where α_1 and α_2 are constants such that $\alpha_1 \geq \alpha_2$. With this definition of stress, the effective normal stress is a function of space and time $\sigma_n^{'}(\boldsymbol{x}, t) = \sigma_n(\boldsymbol{x}) + P(\boldsymbol{x}, t)$, where the normal stress is a function of space and fracture orientation but is frozen in time, and pressure $P(x, t)$ varies with both space and time. Using this sign convention, the effective stress is negative (i.e. compressive), and effective normal stress increases towards a value of zero as the pore pressure increases towards a value of $-\sigma_n$. This formulation falls short of fully-coupled hydro-mechanics, but is still useful in tracking when the MC criteria is satisfied and the evolution of hydraulic diffusivity as a function of stress and pressure.

3.2 Flow in Porous Matrix and Fractures

Single-phase flow through the porous matrix is governed by the groundwater flow equation, which can be written as:

$$\frac{\partial(\rho\phi)}{\partial t} - \nabla \cdot \left(\frac{\rho k}{\mu} \nabla (P + \rho g z) \right) = Q_m \tag{3}$$

where P, z, and Q_m represent fluid pressure, the elevation, and fluid sources/sinks in the matrix, respectively.

Flow through a parallel-plate fracture can be described using the local cubic law for transmissivity (Zimmerman & Bodvarsson, 1996; Murphy et al., 2004; Chaudhuri et

al., 2013):

$$\frac{\partial(\rho b)}{\partial t} - \nabla \cdot \left(\frac{\rho b^3}{12 f \mu} \nabla (P + \rho g z) \right) = Q_f - L_{m-f} \tag{4}$$

where f is a coefficient that is generally greater than or equal to unity that accounts for fracture roughness (Witherspoon et al., 1980), Q_f is a source/sink term normalized by fracture height, and L_{m-f} is the leakoff mass flux per unit area from the fracture to the matrix. Eq. 4 is a 2D representation of the conservation of mass per unit fracture width, perpendicular to the direction of flow and the aperture. In an approach where the fracture and matrix are treated as separate domains, the pressure from the fracture domain would be treated as a boundary condition to the matrix domain, and the pressures within the matrix domain would be used to calculate the leakoff flux as a function of the local pressure difference across the fracture-matrix interface. The leakoff flux would need to be represented as a sink term in the fracture domain.

PFLOTRAN is a massively-parallel, control-volume, subsurface flow and transport code that solves Eq. 3. We take advantage of PFLOTRAN's (Lichtner et al., 2019a; Hammond et al., 2014; Lichtner et al., 2019b) parallel features and robust computational algorithms to simulate large domains with large property contrasts, which requires that we treat the fractures and matrix as a single domain rather than two. With such an approach, a single computational grid is employed encompassing fracture and matrix blocks. The conditions at fracture-matrix interfaces are automatically accounted for consistently in a finite volume approach that represents fluxes across adjacent nodes based on local pressure gradients. Leakoff fluxes are thus naturally calculated based on the local pressure gradients across interfaces between fracture and matrix blocks, and do not need to be represented explicitly as a sink term. To correctly capture the physics of fracture flow within the formulation employed by PFLOTRAN, the following fracture relationships can be introduced for porosity and permeability (Birdsell et al., 2015; Chaudhuri et al., 2013; Pandey et al., 2017; Bower & Zyvoloski, 1997):

$$\phi = \frac{b}{b_p} \phi_\tau \tag{5}$$

$$k = \frac{b^3}{12 b_p f} k_\tau \tag{6}$$

where b_p is the grid block dimension in the direction normal to the fracture, ϕ_τ and k_τ are porosity and permeability multipliers that are equal to 1 prior to shear failure and experience a step change when MC shear failure occurs along a fracture or fault. Eq. 5 assumes that the change in fluid storage within the grid block is primarily due to fracture deformation. Eq. 6 assumes that the grid block permeability is dominated by fractures. These assumptions are valid for flow in basement fractures because they are much more permeable and compressible than the intact crystalline rock (especially for low-compressibility rock and with small values of b_p). When Eq. 5 and 6 are brought into Eq. 3, and a single-domain computational approach is employed, the modified flow equation for fractures is:

$$\frac{1}{b_p} \frac{\partial(\rho b)}{\partial t} - \nabla \cdot \left(\frac{\rho b^3}{12 b_p f \mu} \nabla (P + \rho g z) \right) = Q_m \tag{7}$$

which is identical to Eq. 4 divided by the grid block dimension (b_p) and adjusted to a 3D feature so that Q_m is used instead of Q_f and L_{m-f} is not explicitly included because leakoff is naturally calculated in the single domain approach. This approach has been employed in several previous works (Birdsell et al., 2015; Chaudhuri et al., 2013; Pandey et al., 2017).

We solve the equations of flow in the matrix (Eq. 3) and fractures (Eq. 7) using PFLOTRAN by utilizing the traditional definitions of porosity and permeability in the matrix grid blocks and Eq. 5 and 6 in the fracture grid blocks. This approach correctly

captures the physics of flow within fractures, leakoff to matrix, and flow within the matrix. The fluid properties (i.e. ρ and μ) and the porosity in the storage term are functions of pressure and are updated iteratively within a Newton-Krylov iteration employed by PFLOTRAN in each time step. The porosity in the fracture block is defined in Eq. 5, while the porosity in the matrix is defined as $\phi = \beta_m(P - P_o) + \phi_o$ where β_m is the matrix compressibility, ϕ_o is the porosity at the reference pressure P_o (Birdsell, Karra, & Rajaram, 2018). Note that fracture deformation, i.e. variation in b as a function of effective stress, is described in Sec. 3.3. For implementation reasons, the permeability term shown in Eq. 6 is lagged by one time step in the fracture grid blocks, and it is important to take small enough time-steps that this lagging does not affect the results. To ensure that the time step size employed in Sec. 5 is appropriate, we carried out convergence studies showing that results were unchanged with smaller time steps. The DFNM approach consistently represents the physics of fracture and matrix flow, including leakoff, while taking advantage of an existing, efficient subsurface flow code. Additionally, it allows the hydraulic diffusivity to be updated as mechanical deformations alter b, as discussed in the next section.

3.3 Hydraulic Diffusivity as a Function of Fracture Deformation

The hydraulic diffusivity of fractured rock changes as fractures experience mechanical deformations (Sec. 2.2). There are at least two ways that hydraulic diffusivity can be altered in the context of IIS. The first is via normal deformation on fractures/faults, which alters b and therefore ϕ and k (Eq. 5 and 6). The second is via shear deformation, which can have a range of effects on porosity and permeability, which are modeled by ϕ_τ and k_τ in Eq. 5 and 6. This section presents the relationships used to model the influence of normal and shear deformation on the hydraulic diffusivity of fractures within the DFNM-MC approach.

3.3.1 The Influence of Normal Deformation on Hydraulic Diffusivity

We use the Bandis et al. (1983) constitutive relationship to relate the fracture aperture to the effective normal stress:

$$b = b_{max} + \frac{A\sigma_n^{'}}{1 - B\sigma_n^{'}} \tag{8}$$

where b_{max} is the aperture when $\sigma_n^{'} = 0$ and A and B are parameters. $\sigma_n^{'}$ is negative at the depths of IIS because the magnitude of compressive normal stress is larger than the magnitude of pore pressure (see Sec. 3.1). A is the inverse of the initial fracture stiffness, K_{ni}, at $\sigma_n^{'} = 0$ (i.e. $1/A = K_{ni} = \partial\sigma_n^{'}/\partial b$). $A/B = b_{max} - b_{min}$ where b_{min} is the fracture aperture as $\sigma_n^{'} \rightarrow -\infty$. As originally measured in the lab, the Bandis model applies to the mechanical fracture aperture, but it has also been used to describe hydraulic aperture (Murphy et al., 2004; Pandey et al., 2017). In our partially-coupled hydro-mechanical model, the stress is a function of space and the pore pressure is a function of space and time. Therefore the Bandis relationship implies an initial aperture field based on the stress state, the initial pressure, and the fracture orientation. Subsequently, the aperture field can evolve with time as the pore pressure changes throughout the simulation, and fractures are pressurized.

3.3.2 The Influence of Shear Deformation on Hydraulic Diffusivity

In addition to deforming in the normal direction, fractures and faults can fail in shear. One model that describes when shear failure will occur is the MC failure criterion:

$$c_0 - \mu_f\sigma_n^{'} - |\boldsymbol{\tau}| \leq 0 \tag{9}$$

where c_0 is the fault cohesion and μ_f is the coefficient of friction. Fracture and fault permeability can be enhanced by up to two orders of magnitude due to shear failure (Evans et al., 2005; Rutqvist et al., 2007; Kelkar et al., 2014). Studies of asperity-scale shear processes suggest that the permeability enhancement within the fracture may be anisotropic (Mallikamas & Rajaram, 2005; Lang et al., 2018), but we follow previous reservoir-scale work in assuming that the permeability enhancement within the fracture is isotropic (Kelkar et al., 2014). Even though porosity may change due to shear failure, it is likely to be much smaller than the change in permeability because the increase in permeability after shearing is at least partially due to changes in the aperture correlation structure, which has a smaller influence on porosity (Mallikamas & Rajaram, 2005). In our model, we assume that permeability increases as a step change after Mohr-Coulomb failure, without a change in porosity (i.e. $k_\tau \geq 1.0$ and $\phi_\tau = 1.0$ after Mohr-Coulomb failure in Eq. 5 and 6). These assumptions have also been made by previous modeling studies (Rutqvist et al., 2007; Kelkar et al., 2011).

4 Conceptual and Numerical Model

In this section, we describe the conceptual and numerical model, the fracture generation algorithm, the initial and boundary conditions, and the simulation scenarios that are presented in the results section (Sec. 5). We chose our conceptual and numerical model based on an approximate representation of the IIS site near Greeley, CO. There are two reasons for doing this: (a) because it allows us to compare a DFNM-MC model to a previous EPM-TP study at a well-characterized site, and (b) because the Greeley site has many similarities with other IIS sites in the U.S., and therefore the results will be representative of many areas of IIS.

4.1 Greeley, Colorado IIS

Our conceptual and numerical model is shown in Fig. 1. While there are many disposal wells near the Greeley swarm, the NGL-C4A well has received the most attention due to its large injection volumes and its spatio-temporal correlation with the seismicity (Brown et al., 2017; W. L. Yeck et al., 2016). It is drilled into a 500-m thick group of formations that are primarily permeable sandstone with lesser amounts of carbonate and shale, which are overlain by a mudstone confining layer and underlain by critically-stressed crystalline basement. The NGL-C4A well started injecting approximately one year prior to the M_w 3.2 earthquake in June 2014 at an average rate of $\sim 5{\cdot}10^5$ m^3/yr. After the earthquake, injection was briefly halted and remedial cement was added in the hope that it would hydraulically isolate the well from the basement. Seismicity was monitored as the injection rate was increased to near the pre-earthquake value. Nevertheless, another felt sequence occurred in August 2016, approximately 3 years after injection originally began.

Some parameters at the Greeley site are well known. For example, the injection formation permeability has been measured at the core scale and the field scale (Brown et al., 2017). General estimates of the matrix compressibility (β_m) and porosity (ϕ), which affect the hydraulic diffusivity by contributing to the storage term, are available for sandstone, mudstone, and fractured crystalline rock (Freeze & Cherry, 1979). The injection formation is fractured toward the bottom. These fractures could hydraulically connect the injection formation to the basement, which is also fractured (W. Yeck et al., 2016). The most uncertain parameter in this hydrologic system is the permeability of the basement fracture/matrix system. The uncertainty in basement permeability is due to uncertainty in the number, size, connectivity, and hydraulic properties of basement fractures and faults, which dominate the permeability. Due to the uncertainties in fracture properties, fractures are randomly generated (see Sec. 4.2). There is also uncertainty in the permeability of the unfractured basement rock, and we assume a value at the upper-

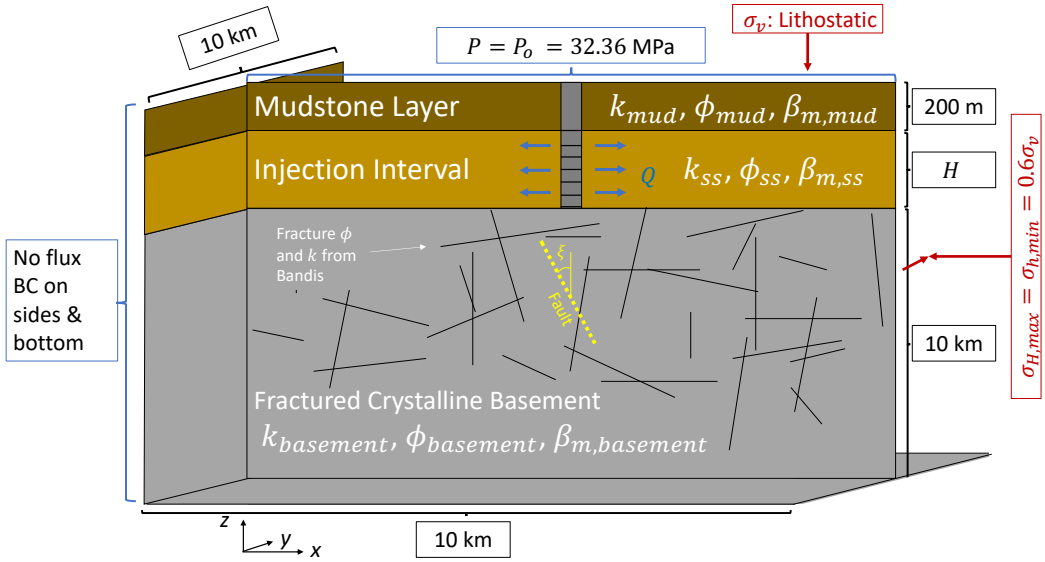

Figure 1. Conceptual model and boundary conditions. The domain size is 10 km in the x and y directions and $(10.2 + H)$ km in the z direction. H is the aquifer height and equals 0.5 km for the simulations in Sec. 5.1 and 0.4 m in Sec. 5.2. Hydrologic boundary conditions and the well source term are illustrated in blue. Injection takes place at $x = y = 5.0$ km, $10.0 \leq z \leq 10.0 + H$ km. The stress state is illustrated in red. Rock properties are indicated on the figure with subscripts "mud", "ss", and "basement" for the mudstone confining layer, the sandstone injection interval, and the in-tact basement rock, respectively. Fractures are indicated schematically with black lines. Fractures (and the fault in Sec. 5.2) are assigned porosity, permeability, and aperture based on Eq. 5, 6, and 8, respectively. The yellow dashed line illustrates a deterministically-located fault that is used in the sensitivity analysis in Sec. 5.2. ξ is the angle between the maximum principal stress (i.e. the vertical stress σ_v) and the fault, which is selected so that the fault is optimally- or suboptimally-oriented. Figure is modified from Birdsell, Rajaram, and Karra (2018).

end of unfractured metamorphic and igneous rocks (Freeze & Cherry, 1979). The parameters used in the DFNM-MC simulations in Sec. 5 are reported in Table 2.

4.2 Fracture Generation Algorithm

Given the uncertainties in fracture locations and properties, fractures are generated from statistical distributions. The distance between subsequently-generated fracture centers is taken from a power law distribution, and the direction between subsequently-generated fracture centers is randomly chosen. If the entire fracture falls outside of the domain, a new fracture location is randomly chosen within the basement. We generate fracture orientations from three equally-probable fracture families that point north-south, east-west, and horizontally. Within each family, there is also variation in the orientation according to a von Mises-Fisher distribution (Wood, 1994). Fractures are idealized as circles of radius r which are generated from a truncated power law distribution (Hyman et al., 2015)

$$r = r_o \left[1 - u + u \left(\frac{r_o}{r_u} \right)^{\alpha_r} \right] \tag{10}$$

Table 2. Simulation parameters for the DFNM-MC simulations presented in Sec. 5.1. Note that the fracture permeability and porosity are not directly reported in this table, but can be calculated from the effective stress, the parameters in this table, and Eq. 5 and 6. The parameters in scenarios EPM1, EPM2, and EPM3 in Sec. 5.1 are the same as in this table except for $k_{basement}$ and $\beta_{m,basement}$, which were adjusted to account for the equivalent permeability and compressibility (see Table 3). Most of the parameters remain the same in the sensitivity analysis (Sec. 5.2), except: (a) the grid dimension, b_p, is increased to 200 m and the aquifer thickness, H, is reduced to 400 m to decrease computational cost; (b) the simulation duration, t, is increased to 10 yr to investigate longer-term disposal; and (c) the number of fractures is varied in the sensitivity analysis.

Variable	Description	Value	Unit
H	Aquifer thickness[a]	500	m
b_p	Grid block size[a]	100	m
k_{mud}	Permeability of confining layer	10^{-17}	m^2
k_{ss}	Permeability of injection interval	$4 \cdot 10^{-14}$	m^2
$k_{basement}$	Permeability of basement matrix	10^{-17}	m^2
ϕ_{mud}	Porosity of confining layer	0.2	
ϕ_{ss}	Porosity of injection interval	0.25	
$\phi_{basement}$	Porosity of basement matrix	0.05	
$\beta_{m,mud}$	Confining layer compressibility	10^{-8}	Pa^{-1}
$\beta_{m,ss}$	Injection interval compressibility	10^{-8}	Pa^{-1}
β_f	Fluid compressibility	$4.4 \cdot 10^{-10}$	Pa^{-1}
μ	Fluid viscosity	$8.9{\cdot}10^{-4}$	Pa-s
P_o	Reference pressure (Eq. 12-14; Fig. 1)	32.36	MPa
$\rho_{f,o}$	Reference density (Eq. 12-14)	1100	kg/m^3
d_o	Reference depth (Eq. 12-14)	3000	m
$\sigma_{v,o}$	Vertical stress at top of domain	-73.55	MPa
$\rho_{s,o}$	Rock density at top of domain	2500	kg/m^3
β_s	Compressibility of solid rock grains	$1.8 \cdot 10^{-10}$	Pa^{-1}
Q	Injection rate	$5 \cdot 10^8$	kg/yr
-	Injection location	$x = y = 5.0,\ 10.0 \leq z \leq 10.5$	km
t	Injection and simulation duration[b]	3	yr
n_{frac}	Number of fractures[c]	2000	
f	Fracture coefficient (Eq. 6)	1	
r_o	Minimum fracture radius (Eq. 10)	300	m
r_u	Maximum fracture radius (Eq. 10)	1000	m
α_r	Power law exponent (Eq. 10)	2.5	
A	Bandis parameter (Eq. 8)	10^{-11}	m/Pa
b_{min}	Minimum fracture aperture	$2 \cdot 10^{-4}$	m
$\Delta b_{max,range}$	Range of maximum aperture (Eq. 11)	$2 \cdot 10^{-4}$	m
$b_{max,o}$	Reference maximum aperture (Eq. 11)	$3 \cdot 10^{-4}$	m
α_1	Multiplier for $\sigma_{H,max}$ (Sec. 3.1)	0.6	
α_2	Multiplier for $\sigma_{h,min}$ (Sec. 3.1)	0.6	
c_0	Fault cohesion (Eq. 9)	0.0	Pa
μ_f	Coefficient of friction (Eq. 9)	0.67	

[a] Altered in Sec. 5.2 to reduce computational cost.
[b] Altered in Sec. 5.2 to investigate longer injection.
[c] $n_{frac} = 1000$ for base case in Sec. 5.2.

where r_o is the minimum radius, r_u is the maximum radius, α_r is the power-law exponent, and u is a uniform random variable between 0 and 1. The maximum fracture aperture, b_{max} in Eq. 8, is correlated to the fracture radius according to Eq. 11

$$b_{max} = b_{max,o} + \frac{r - r_o}{r_u - r_o} \Delta b_{max,range} \tag{11}$$

where $b_{max,o}$ is the maximum aperture for a fracture of length r_o and $\Delta b_{max,range}$ is the range over which b_{max} can vary. We assume fixed values for A and b_{min}, calculate b_{max} for each fracture with Eq. 11, and set $B = A/(b_{max} - b_{min})$.

To work with the DFNM-MC approach, fractures and their properties are mapped to the continuum grid. To capture the permeability anisotropy of fractures, so that flow goes more readily along fractures than perpendicular to them, it is important that $r_o > b_p$ and that the fracture permeability is much, much larger than the matrix permeability. (Both of these criteria are satisfied for the simulations presented in this paper.) Under these assumptions, we can assign an isotropic permeability value to the fractured grid blocks and trust that the fracture/matrix system heterogeneity will generate anisotropic behavior. We acknowledge that approaches using lower-dimensional fracture elements reproduce the fracture permeability anisotropy better than our approach (e.g. Jin and Zoback (2017, 2018); Ucar et al. (2018); Jha and Juanes (2014)), but note that our approach still allows for leakoff into the surrounding matrix, and is a relatively good approximation of the permeability tensor of a fracture/matrix system (see Supplementary Text S1 and Fig. S1). At grid cells where multiple fractures intersect, the properties of the fracture that is most favorably-oriented for MC failure are used. This ensures that the model will experience seismicity at the value of ΔP that corresponds to the smallest ΔP_c of the fractures within the grid block.

4.3 Initial and Boundary Conditions Corresponding to a Critically-Stressed Basement

In this study, we interpret a critically-stressed rock to be one in which the critical pressure increment required for MC failure *on an optimally-oriented fracture* is less than or equal to 0.1 MPa, while the majority of fractures will require a larger pressure increase to experience MC failure. Therefore we refer to the "minimum critical pressure" ($\Delta P_{c,min}$) as the pressure increase that is required to cause an earthquake on an optimally-oriented fracture. In reality, the initial conditions of stress and pressure: (1) increase with depth so that $\Delta P_{c,min}$ may be a function of depth, and (2) vary horizontally at a given depth so that $\Delta P_{c,min}$ may also vary horizontally. We assume that there are no variations in the horizontal initial conditions so that $\Delta P_{c,min}$ is a function of depth but not lateral position. As discussed in the following paragraphs, we select initial conditions and material parameters such that $\Delta P_{c,min} = 0.05$ MPa at the top of the basement, increases to a maximum of 0.1 MPa at 4 km BTB, and slowly decreases at greater depths. We refer to these minimum and maximum values of minimum critical pressure as $\Delta P_{c,min1} = 0.05$ MPa and $\Delta P_{c,min2} = 0.1$ MPa, respectively. The in-situ stress state, initial pressure, and material parameters are chosen carefully so that the basement is critically stressed initially, which allows our DFNM-MC simulation results to be compared to previous EPM-TP models that assumed $TP \approx 0.1$ MPa.

The initial pore pressure is assumed hydrostatic, which for a compressible fluid can be described as:

$$P(d) = P_o + \int_{d_o}^{d} \rho_f(d) g dz \tag{12}$$

$$P_o = \rho_{f,o} g d_o \tag{13}$$

$$\rho_f(d) = \rho_{f,o} \exp\left(\beta_f (P(d) - P_o)\right) \tag{14}$$

where d is the depth below ground surface, $\rho_{f,o}$ is the reference fluid density (assumed to be 1100 kg/m^3), and P_o is the reference fluid pressure at the reference depth d_o = 3000 m, which is taken as the top of the domain. The vertical stress is similarly assumed to follow a lithostatic stress profile:

$$\sigma_v(d) = \sigma_{v,o} + \int_{d_o}^{d} \rho_s(d) g dz \tag{15}$$

$$\sigma_{v,o} = \rho_{s,o} g d_o \tag{16}$$

$$\rho_s(d) = \sigma_{v,o} \exp \beta_s (\sigma_v(d) - \sigma_{v,o}) \tag{17}$$

where ρ_s is the solid rock grain density, $\rho_{s,o}$ and $\sigma_{v,o}$ are the reference rock density and vertical stress at the top of the domain, and β_s is the compressibility of the solid rock grains. Eq. 17 was chosen for convenience, but solid density could be expressed more generally in terms of all three principal components of stress (i.e. σ_v, $\sigma_{H,max}$, and $\sigma_{h,min}$), and it could also account for the different rock types (e.g. mudstone, sandstone, and basement rock). Nevertheless since the horizontal stresses are also a function of the vertical stress, the use of Eq. 17 is a reasonable approximation, and the mudstone and sandstone layers are thin enough that including different rock types would have a small effect on the stress state. For the simulations presented in this paper, we assume that the multipliers for the horizontal stresses are $\alpha_1 = \alpha_2 = 0.6$ (see Sec. 3.1), which is consistent with the apparent normal faulting regime near Greeley, CO (Brown et al., 2017). By calculating $\Delta P_{c,min}$ as a function of depth at many combinations of parameter values, we selected parameter values as: $\mu_f = 0.67$, $\rho_{s,o} = 2500$ kg/m^3, and $\beta_s = 1.8 \cdot 10^{-10}$ Pa^{-1}. The values of μ_f and $\rho_{s,o}$ fall within their accepted ranges, and β_s is approximately ten times larger than for perfectly intact granite rock (De Marsily, 1986). These rock and fault parameter values, along with the assumed values for hydrostatic pressure, ensure that our definition of a critically-stressed basement is satisfied (i.e. $\Delta P_{c,min} \leq$ 0.1 MPa). Even though the value of β_s is larger than the literature value, and the combination of fault, stress, and pressure parameters are not unique, Eq. 12-17 create an initial pressure and stress condition that allows for comparison to previous EPM-TP modeling studies that assumed $TP \approx 0.1$ MPa as an earthquake-triggering condition. Note that the compressibility of the solid rock grains is typically much, much smaller than the matrix compressibility (i.e. $\beta_s << \beta_m$) and has a minimal contribution to the hydraulic diffusivity, which is why Eq. 1 can be written without β_s (Birdsell, Karra, & Rajaram, 2018). For this same reason, our selected value of β_s does not alter the hydraulic diffusivity to an unrealistic value, and the value of β_s is only relevant to specify an initial stress condition.

The boundary conditions are simpler to specify than the initial conditions. The pore pressure along the top of the domain is fixed to $P = P_o = 32.26$ MPa. The remaining boundaries are no flux boundaries, and are sufficiently far from the injection well to minimize boundary effects. The well acts as a mass source of $Q = 5 \cdot 10^8$ kg/yr, based on the average injection rate of the NGL-C4A well. The stresses are specified everywhere within the domain initially, but mechanical boundary conditions do not need to be specified since the stresses and strains are not explicitly calculated in our partially-coupled approach (see Sec. 3.1).

4.4 Scenarios Simulated

The results are broken down into two parts in the next section: (a) Sec. 5.1 presents a comparison between DFNM-MC and EPM-TP modeling frameworks, and (b) Sec. 5.2 presents a sensitivity analysis using the DFNM-MC approach.

We follow the general simulation setup of Brown et al. (2017) in our comparison of the DFNM-MC approach and the EPM-TP approach, and we choose parameters for the DFNM-MC simulation to readily facilitate a comparison to Brown et al. (2017). We present one DFNM-MC simulation and three EPM-TP simulations. The DFNM-MC scenario has 2000 total fractures, with 1727 falling entirely within the domain and the remainder falling partially outside of the domain. The total fracture area is 10^9 m^2. The parameter differences between the three EPM scenarios in Sec. 5.1 are shown in Table 3. The first EPM scenario (EPM1) provides the most direct comparison to the DFNM simulation. It employs a value of basement compressibility that accounts for the compliant fractures ($\beta_m = 10^{-9}$ Pa^{-1}). It also employs an equivalent permeability that accounts for the presence of fractures in the DFNM simulation, wherein the principal components of the permeability tensor in the x, y, and z direction are $k_{eff,x} = 2.4 \cdot 10^{-16}$ m^2, $k_{eff,y} = 1.7 \cdot 10^{-16}$ m^2, and $k_{eff,z} = 3.4 \cdot 10^{-16}$ m^2, respectively. Note that we calculated the equivalent permeability using three numerical permeameter tests on the DFNM model. This was achieved by specifying a known pressure gradient at two opposing faces of the domain, numerically calculating the steady-state flow rate, and then back-calculating the relevant component of the permeability tensor using Darcy's equation. We assumed that the principal axes of the permeability tensor lined up with the x, y, and z directions. We note that the degree of anisotropy is relatively minor and can be explained by the randomness of the fracture network. The hydraulic diffusivity in EPM1 is $c \approx 2{\cdot}10^{-4}$ m^2/s, which falls within the range of c_{bulk} in Table 1. The second EPM scenario (EPM2) used the hydrologic parameters from Brown et al. (2017), including an exponentially-decreasing permeability and an incompressible basement rock matrix so that changes in fluid storage are only due to fluid compressibility. This corresponds to a hydraulic diffusivity value of $c \approx 2$ m^2/s at the top of the basement, which decreases with depth. The third EPM scenario (EPM3) uses the same permeability as Brown et al. (2017), with the compressibility of fractured basement rock as in the first EPM scenario (i.e. $\beta_m = 10^{-9}$ Pa^{-1}). In this scenario the hydraulic diffusivity $c \approx 0.04$ m^2/s. The simulation duration, t, is three years and involves injection at the average flow rate of the NGL-C4A well from the summer of 2013 to the summer of 2016 .

In Sec. 5.2, we present a sensitivity analysis to understand how fracture density, the orientation of a deterministically-located fault, and the nonlinear hydraulic diffusivity of fractures and faults affect the likelihood of IIS. This sensitivity analysis helps us understand how elevated pressure and seismicity can reach seismogenic depths (≥ 2 km BTB). We assume that there is a deterministically-located fault centered 2.0 km below the well (see Fig. 1) that is large enough to host a felt and potentially-damaging earthquake according to earthquake scaling laws and the Modified Mercalli Intensity scale. The fault radius is 1.5 km. The base-case scenario has 1000 fractures and an optimally-oriented fault. The minimum and maximum depth of the fault are 700 m and 3300 m BTB, respectively. To investigate fracture density, the number of fractures, n_{fracs}, is altered to be 100, 500, 1000, 2000, and 4000. Since fracture networks are generated randomly, simulations were performed on 20 realizations for each fracture density. To investigate the potential for optimally- and suboptimally-oriented faults to host IIS, several fault orientations are considered. Note the optimal orientation can be calculated in 2D since the horizontal components of stress are equal in our simulations. This is done by first calculating the friction angle from the coefficient of friction: $\kappa = \arctan(\mu_f) \cdot (180^\circ/\pi) = 33.8^\circ$, and then calculating the angle between $\sigma_1 = \sigma_v$ and the fault plane as: $\xi = 45^\circ - \kappa/2 = 28.1^\circ$ (see Fig. 1) (Einstein & Dershowitz, 1990). The calculation of optimal orientation can be expanded to 3D if the horizontal components of stress are

Table 3. The source and value of parameters used in the three EPM modeling scenarios investigated in Sec. 5.1. EPM1 represents the fairest comparison to the DFNM simulation because it uses permeability from a numerical permeameter test and a reasonable value of $\beta_{m,basement}$. EPM2 uses the Brown et al. (2017) parameters, including an unrealistically-small value of $\beta_{m,basement}$. EPM3 uses the Brown et al. (2017) permeability and a reasonable value of $\beta_{m,basement}$.

Variable	EPM1	EPM2	EPM3
$k_{basement}$ (m^2)	$\approx 2 \cdot 10^{-16}$	$4 \cdot 10^{-14}$ – $1 \cdot 10^{-18}$	$4 \cdot 10^{-14}$ – $1 \cdot 10^{-18}$
$k_{basement}$ source	Numerical permeameter	Brown et al. (2017)	Brown et al. (2017)
$\beta_{m,basement}$ (Pa^{-1})	10^{-9}	0	10^{-9}
$\beta_{m,basement}$ source	Freeze and Cherry (1979)	Brown et al. (2017)	Freeze and Cherry (1979)
c m^2/s	$\approx 2 \cdot 10^{-4}$	≈ 2, decreasing with depth	≈ 0.04, decreasing with depth

[a]Brown EPM model uses smaller β_m.

Table 4. Scenarios for the sensitivity analysis shown in Sec. 5.2.3. The sensitivity analysis explores the fracture/fault constitutive relationships that describe how deformations alter the hydraulic diffusivity. "MC-Bandis" includes permeability enhancement due to shear dilation after MC failure and permeability and porosity that are functions of normal deformation as described by the Bandis et al. (1983) constitutive relationship. "Bandis" turns off the permeability enhancement due to MC failure, and "Constant" turns off all the hydraulic diffusivity alterations due to MC and Bandis, although the Bandis relationship is used to assign the initial fracture parameters.

Variable	MC-Bandis	Bandis	Constant
k, fract.	Eq. 6	Eq. 6	Eq. 6 at I.C.
k_τ, after MC shear	10	1	N/A
ϕ, fract.	Eq. 5	Eq. 5	Eq. 5 at I.C.
ϕ_τ, after MC shear	1	1	N/A

not equal. The variation from optimal orientation, $\Delta\xi$, is altered in the sensitivity analysis by 0°, $\pm1^\circ$, and $\pm2^\circ$, where positive angles indicate that the fault is inclined further towards the horizontal. To investigate the importance of the hydraulic diffusivity constitutive relationships (i.e. Bandis and MC) on IIS, we simulate a scenario where MC shear failure and Bandis normal deformation alter the hydraulic diffusivity ("MC-Bandis"), one where only Bandis normal deformation alters the hydraulic diffusivity ("Bandis"), and one where the hydraulic diffusivity is invariant in time throughout the simulation ("Constant"). Note that for the invariant hydraulic diffusivity case, there is still a difference between c in the fractures and the matrix, but c in the fracture stays constant in time throughout the simulation. These three scenarios are summarized in Table 4. It is worth noting that in simulations where fault orientation and hydraulic diffusivity are altered, the same underlying fracture networks are used (i.e. the twenty sets of 1000 fractures that were generated to investigate fracture density were not re-generated). Some parameters in the sensitivity analysis are changed from their values in Sec. 5.1 and Table 2 to reduce computational costs and allow for hundreds of simulations. The grid block size is increased to $b_p = 200$ m, the aquifer thickness is reduced from $H = 500$ m to $H = 400$ m, and the injection and simulation duration, t, is increased to ten years to investigate longer-term pore pressure diffusion, which is relevant for many disposal wells.

5 Results

5.1 Comparison Between DFNM-MC and EPM-TP Approaches

This section focuses on evaluating the differences in behavior between the DFNM-MC approach and the EPM-TP approach as applied to the IIS near Greeley, CO (Sec. 4.1 and 4.4). Fig. 2(a) shows all the fractures in the DFNM-MC domain, colored by permeability. Fig. 2(b) shows a three-dimensional plot of fractures that experienced MC failure (i.e. seismicity) in the DFNM-MC simulation. The maximum depth of seismicity was only 900 m BTB, not ≥ 2000 m BTB that we would expect from field observations. However, $\Delta P_{c,min}$ did reach seismogenic depths as discussed in the next paragraph. In Sec. 5.2 we explore the factors that contribute to $\Delta P_{c,min}$ and seismicity at greater depths.

Fig. 3 shows a three-dimensional view of the extent of critical pressure propagation for the DFNM-MC and the EPM-TP simulations. Regions where $\Delta P < \Delta P_{c,min1} = 0.05$ MPa are removed from the figure because these regions cannot experience earthquakes. Regions where $\Delta P \geq \Delta P_{c,min2} = 0.10$ MPa are colored red. Optimally-oriented

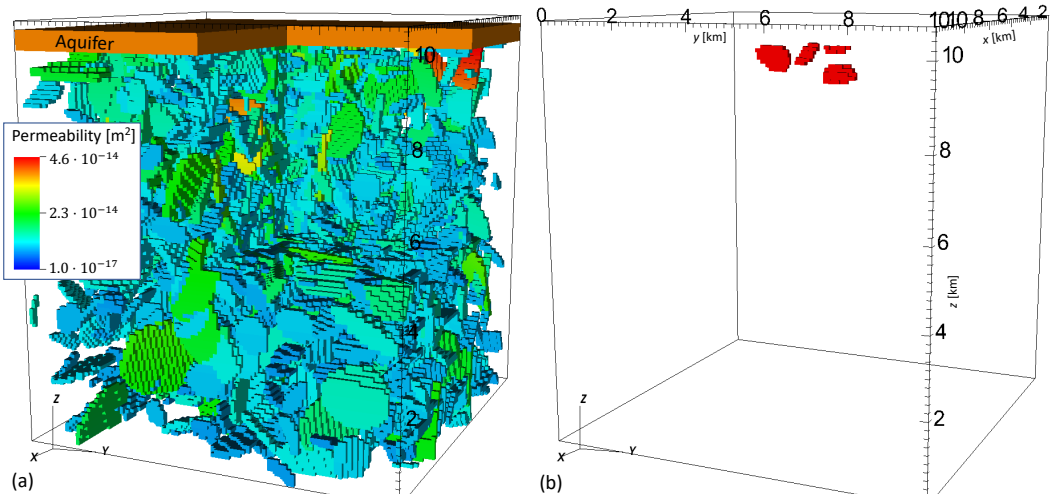

Figure 2. Illustration of the fracture network. Fig. (a) shows the initial permeability for all the regions within the domain that have $k > 10^{-17}$ m^2, which includes all the fractures and the sandstone aquifer near the top of the domain. The regions with $k \leq 10^{-17}$ m^2 (i.e. the unfractured basement and the overlying confining unit) are filtered out of the figure. There is a cutaway at $x = y = z = 5000$ m. Fig. (b) shows fractures that experienced Mohr-Coulomb failure, which is assumed to indicate seismicity.

fractures will experience MC failure between $\Delta P_{c,min1}$ and $\Delta P_{c,min2}$. Fig. 4 shows two-dimensional slice plots of pressure change through the $x-z$ plane at $y = 5$ km, in the plane of the well, and Fig. 5 shows slice plots of pressure change through the $x-y$ plane 2.0 km BTB. Fig. 3-5 clearly illustrate that the DFNM-MC model propagates critical pressure farther and more heterogeneously into the basement than the EPM1 scenario whose properties are consistent with the underlying DFNM domain. In fact, the maximum depth of $\Delta P_{c,min1}$ was 2150 m BTB for the DFNM model (Fig. 3(a)-5(a)) while only reaching 450 m for the EPM1 scenario (Fig. 3(b)-5(b)). Like EPM1, the EPM3 scenario (Fig. 3(d)-5(d)) does not propagate TP to depths $\geq$2 km BTB; only the EPM2 scenario (Fig. 3(c)-5(c)), which employs an unrealistically-large hydraulic diffusivity, results in TP below 2 km BTB. It is noteworthy that $\Delta P_{c,min1}$ propagates much deeper (2150 m BTB) than locations of MC failure (900 m BTB) for the DFNM-MC model (compare Figs. 2(b) and 3(a)). This is because only a small fraction of fractures are optimally oriented for MC failure. Other fractures require $\Delta P > \Delta P_{c,min}$ for failure, and therefore the $\Delta P_{c,min}$ front can propagate to greater depths than the seismic front.

5.2 DFNM Sensitivity Analysis

In this section, we perform a sensitivity analysis to understand the combination of parameters that can lead to critical pressure and MC failure at depths that are relevant to IIS (i.e. $\geq$2 km BTB). We vary three independent variables in the sensitivity analysis: the fracture density, the fault orientation, and the hydraulic diffusivity constitutive relationships for the fractures and faults, as discussed in Sec 4.4. We focus on three dependent variables in our results. First, we report the maximum depth that $\Delta P_{c,min1} = 0.05$ MPa reaches in each realization, which we call $d_{\Delta P_c}$. Second, we report the maximum depth of seismicity for each realization, $d_{seismicity}$. Third, we report the maximum depth of an earthquake on the fault (EOF) for each realization, d_{EOF}. Since we are interested in the probability of these occurrences as a function of depth, we define the probability of exceeding critical pressure at a given depth d as $P(d_{\Delta P_c} \geq d)$, the probabil-

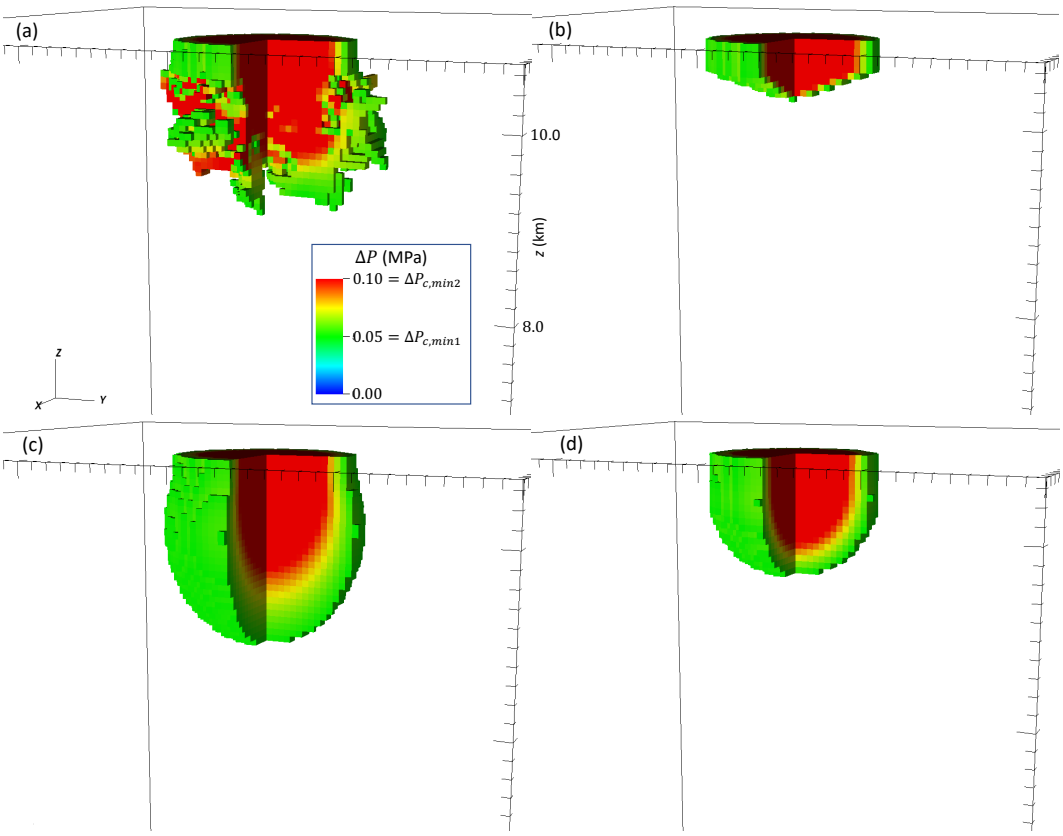

Figure 3. Plot of pressure change for comparison of the extent of critical pressure propagation between the DFNM-MC and EPM-TP models (Sec. 5.1). Regions where $\Delta P < \Delta P_{c,min1} = 0.05$ MPa are not shown because they cannot experience seismicity, and regions where $\Delta P > \Delta P_{c,min2} = 0.1$ MPa are colored red. Fig. (a) is from the DFNM-MC scenario, (b) EPM1, (c) EPM2, and (d) EPM3. The hydraulic diffusivity values in (b) - (d) were $\approx 2 \cdot 10^{-4}$, 2, and .04 m^2/s respectively (Table 3). Comparison between (a) and (b) shows that critical pressure propagates deeper and more heterogeneously in a DFNM-MC model than in an EPM-TP model where the equivalent permeability is based on the underlying DFNM. Comparison between (c) and (d) shows that critical pressure does not propagate as deep when realistic values of compressibility are used.

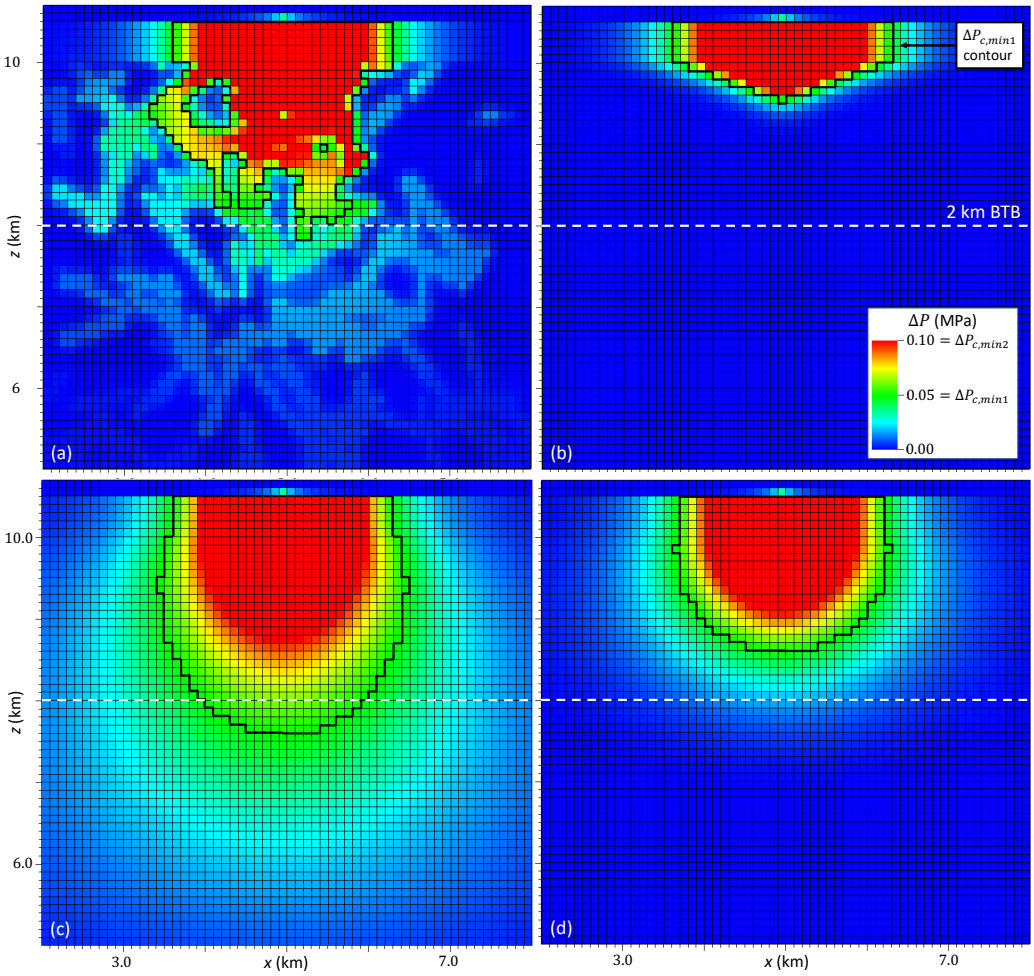

Figure 4. Slice plot of pressure change for comparison of the extent of critical pressure propagation between the DFNM-MC and EPM-TP models (Sec. 5.1). Slices are located in the $x - z$ plane at $y = 5.0$ km, in the plane of the well. Fig. (a) is from the DFNM-MC scenario, (b) EPM1, (c) EPM2, and (d) EPM3. The hydraulic diffusivity values in (b) - (d) were $\approx 2 \cdot 10^{-4}$, 2, and .04 m^2/s, respectively (Table 3). Comparison between (a) and (b) shows that critical pressure propagates deeper and more heterogeneously in a DFNM model than in an EPM model where the equivalent permeability is based on the underlying DFNM. Comparison between (c) and (d) shows that critical pressure does not propagate to 2 km BTB unless porous medium compressibility is neglected. The dashed white line indicates 2 km BTB and the bold black lines indicate the contour of $\Delta P_{c,min1} = 0.05$ MPa.

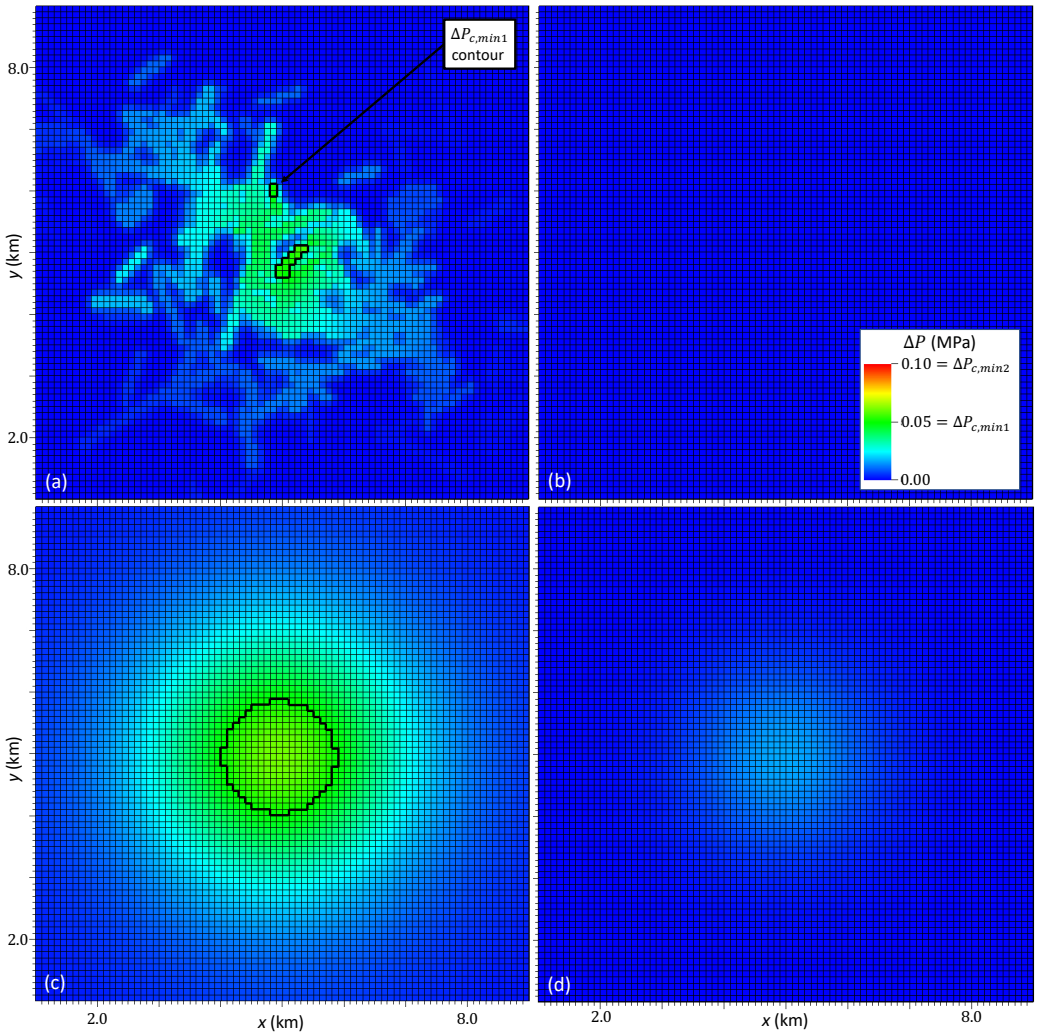

Figure 5. Slice plot of pressure change for comparison of the extent of critical pressure propagation between the DFNM-MC and EPM-TP models (Sec. 5.1). Slices are located in the $x - y$ plane 2 km BTB. Fig. (a) is from the DFNM-MC scenario, (b) EPM1, (c) EPM2, and (d) EPM3. The hydraulic diffusivity values in (b) - (d) were $\approx 2 \cdot 10^{-4}$, 2, and .04 m^2/s, respectively (Table 3). Comparison between (a) and (b) shows that critical pressure propagates deeper and more heterogeneously in a DFNM model than in an EPM model where the equivalent permeability is based on the underlying DFNM. Comparison between (c) and (d) shows that critical pressure does not propagate as deep when a larger value of compressibility is used to account for the fractures. Note the bold black lines indicate the contour of $\Delta P_{c,min1} = 0.05$ MPa in (a) and (c), but do not appear in (b) and (d) because $\Delta P_{c,min1}$ does not reach 2 km BTB.

ity of seismicity exceeding a given depth as $P(d_{seismicity} \geq d)$, and the probability of an EOF exceeding a given depth as $P(d_{EOF} \geq d)$. Twenty realizations are performed for each set of parameter values, and probabilities were calculated as a fraction of the total number of realizations. (Note the data for $d_{\Delta P_c}$, $d_{seismicity}$, and d_{EOF} are reported for each realization in Tables S3 - S5.) There is a lot of overlap between $d_{seismicity}$ and d_{EOF} because the seismicity measure includes the EOF measure, but we elect to show both variables since the earthquake magnitudes of the EOF could be large enough to be felt or even cause damage, while earthquakes on smaller fractures would cause smaller, less-concerning earthquakes. Furthermore, the d_{EOF} measurement shows us the sensitivity of EOFs to fault orientation (Sec. 5.2.2).

5.2.1 Fracture Density

Fig. 6 shows the probability of critical pressure $P(d_{\Delta P_c} \geq d)$, seismicity $P(d_{seismicity} \geq d)$, and EOFs $P(d_{EOF} \geq d)$ as a function of depth and the number of fractures. At shallow depths ($\leq$ 1700 m BTB), the probability of critical pressure increases monotonically with the number of fractures. However at greater depths ($\geq$ 2700 m BTB), there is a non-monotonic relationship, and the probability of critical pressure is largest for intermediate fracture densities. Like critical pressure, the probability of seismicity and EOF generally increased with the number of fractures at shallow depths. However, at depths $\geq$ 2100 m BTB, the probability of seismicity and EOF is highest for an intermediate number of fractures. At depths $\geq$ 1300 m BTB, there is no difference between $d_{seismicity}$ and d_{EOF}. This is likely because: (1) the fault is optimally-oriented and will therefore experience MC failure before fractures at the same depth, which are unlikely to be optimally-oriented, and (2) at these deeper locations a permeable fault is usually acting as the dominant hydraulic pathway, so it will be pressurized before nearby fractures. For depths less than 1300 m BTB the probability of seismicity is greater than the probability of EOF. At these shallower depths fractures can sometimes experience seismicity without the fault experiencing seismicity, especially if the DFN topology does not encourage flow between the disposal well and the fault. Table 5 shows the median, ninetieth percentile, maximum, and standard deviation for $d_{\Delta P_c}$ for each number of fractures. It shows similar trends as Fig. 6(a). Namely, the median $d_{\Delta P_c}$ increases monotonically with the number of fractures, but the ninetieth percentile and maximum $d_{\Delta P_c}$ have a non-monotonic relationship with fracture density. The standard deviation of $d_{\Delta P_c}$ is largest for the intermediate number of fractures.

Physically, there are three broad possibilities for how pressure diffuses from the aquifer through a DFN: First, if the fractures do not hydraulically connect the aquifer to the deep basement, then pressure propagation will be limited to the point where the hydraulic connection dead ends. Second, if many fractures form a dense network of hydraulic connections, then pressure will diffuse into the basement pseudo-spherically. This allows pressure to propagate readily into the basement, but the distance of propagation is still somewhat limited because multiple hydraulic pathways compete for flow and no isolated preferential pathway is established. Third, if fractures/faults form a single preferential pathway into the basement, then pressure can diffuse down the pathway with limited competition from other fractures. This can result in the deepest pressure propagation. These three possibilities of pressure diffusion are illustrated in Fig. 7, which shows the spatial distribution of $\Delta P_{c,min}$ for the fracture-density sensitivity analysis. For each set of realizations with a given number of fractures, three results are shown: one from the realization with the median $d_{\Delta P_c}$, one from the realization with the ninetieth percentile $d_{\Delta P_c}$, and one from the realization with the maximum $d_{\Delta P_c}$.

When few fractures are present, the likelihood of hydraulic connectivity is low (see Fig. 7 (a), (b), (d) and (e)), although in extremely rare cases it seems that a preferential pathway is established deep into the basement even when there are few fractures (e.g. Figs. 7(c) and (f)). When an intermediate number of fractures are present, either: (1)

poor connectivity can occur or, (2) a preferential pathway deep into the basement can occur. If poor connectivity occurs, pressure could be limited to very shallow depths or could reach intermediate depths (as seen in Fig. 7 (g)), depending upon the depth at which the hydraulic pathway dead ends. In somewhat rarer circumstances, the fractures/fault form a preferential pathway that allows elevated pressure to diffuse very deep into the basement (Figs. 7 (h) and (i)). This explains why the deepest maximum and ninetieth percentile $d_{\Delta P_c}$ occur at the intermediate-density DFN (i.e. 1000 fractures). The intermediate fracture network has the largest standard deviation in $d_{\Delta P_c}$, due to the many possibilities that can occur, which range from a very shallow dead-end pathway to a very deep preferential flow pathway. When the number of fractures is very large, it is likely that pseudo-spherical flow develops (see Figs. 7 (m), (n), and (o)). The randomness within the fracture network becomes less important because many connections between fractures are ensured, and therefore no single connection is very important for the final flow pattern. This results in $d_{\Delta P_c}$ that has a relatively deep median but a relatively small standard deviation, and therefore a low probability of extremely deep $d_{\Delta P_c}$, compared to scenarios with an intermediate number of fractures.

The trends in Fig. 6 and Table 5 can be explained with the physics described in the previous two paragraphs. In the majority of cases, a denser fracture network results in a deeper critical pressure, because the likelihood of a hydraulic pathway dead ending is smaller. However if only the deepest instances of critical pressure propagation are associated with IIS, which seems plausible based on the low fraction of wells that are associated with IIS, then a single or limited number of preferential flow paths are likely to be required. Isolated preferential flow paths are more likely to occur with an intermediate number of fractures. Therefore, we propose that an intermediate-density fracture network is the most likely to lead to IIS. However, we point out that most intermediate-density topologies still do not result in deep propagation of critical pressure. It is only the intermediate-density fracture networks with an ideal topology and vertical connectivity that result in deep critical pressure propagation and the possibility of IIS. Intermediate fracture density and connectivity thus appear to provide highly favorable conditions for deep occurrences of ΔP_c.

5.2.2 Fault Orientation

Fig. 8 shows the probability of critical pressure, seismicity, and EOFs as a function of depth and fault orientation. The depth of critical pressure was relatively insensitive to the fault angle. At depths less than 2300 m BTB, a more vertical fault ($\Delta\xi = -1^\circ$ or $\Delta\xi = -2^\circ$) modestly increased the chance of critical pressure, by providing better hydraulic connectivity to the shallow fracture network. At depths $\geq$ 2900 m, optimally- and nearly-optimally-oriented faults ($\Delta\xi = 0^\circ$ and $\Delta\xi = \pm 1^\circ$) were associated with a higher probability of critical pressure, which is due to their higher chance of MC failure and resulting permeability increase. The probability of seismicity and EOF decreased dramatically with very small deviations ($\Delta\xi = \pm 1, \pm 2^\circ$) from optimal orientation. At 2100 m BTB, the probability of seismicity and EOF decreased from 20% for $\Delta\xi = 0^\circ$ to 10% for $\Delta\xi = 1^\circ$, 5% for $\Delta\xi = -1^\circ$, and 0% for $\Delta\xi = \pm 2^\circ$. At this depth, the pressure change associated with MC failure on the fault was: 0.083 MPa for $\Delta\xi = 0^\circ$, 0.11 MPa for $\Delta\xi = \pm 1^\circ$, and 0.21 MPa for $\Delta\xi = \pm 2^\circ$. An EOF never occurred when the fault was deviated $+2^\circ$. This sensitivity analysis shows that even a small deviation from optimal orientation can preclude seismicity on a fault because it increases the pressure required for Mohr-Coulomb failure above $\Delta P_{c,min}$.

5.2.3 Nonlinear Hydraulic Diffusivity From Fracture Deformation

We also investigated the importance of deformation-induced changes in hydraulic diffusivity in DFNM-MC models (see Table 4 and Sec. 4.4). The "Constant" scenario did not calculate MC failure, so the results for seismicity are not reported. As shown in

Table 5. Statistics for the depth of critical pressure as a function of the number of fractures (Sec. 5.2.1). The table reports the median, ninetieth percentile, maximum, and standard deviation of $d_{\Delta P_c}$ for each number of fractures. Twenty realizations were run for each number of fractions, and the median, ninetieth percentile, and maximum $d_{\Delta P_c}$ correspond to the eleventh, third, and first realization, respectively, ordered from deepest to shallowest $d_{\Delta P_c}$.

Number of fractures	Median $d_{\Delta P_c}$ (m)	Ninetieth percentile $d_{\Delta P_c}$ (m)	Maximum $d_{\Delta P_c}$ (m)	Std. Deviation (m)
100	300	500	3300	670
500	900	1900	3900	930
1000	1500	3900	4300	1300
2000	1700	3500	3700	1020
4000	2500	3300	3500	670

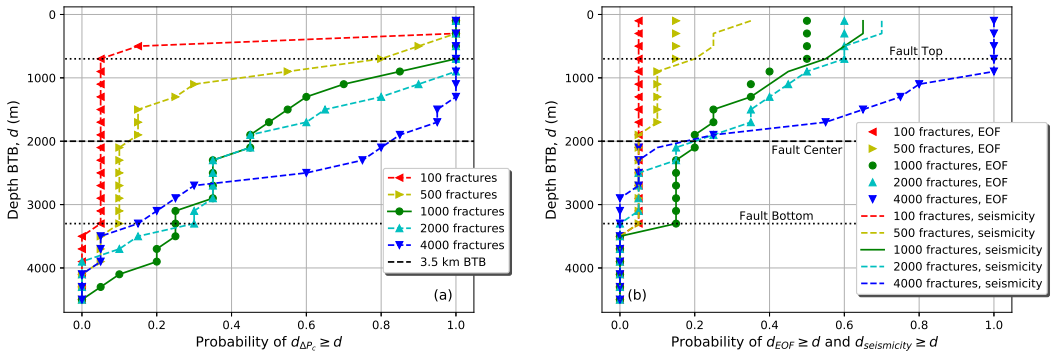

Figure 6. Fig. (a) shows the probability of exceeding critical pressure ($\geq \Delta P_{c,min1} = 0.05$ MPa) as a function of depth and the number of fractures, which is expressed by plotting $P(d_{\Delta P_c} \geq d)$ versus d. The probability of exceeding critical pressure increased monotonically with the number of fractures at shallow depths, whereas at greater depths ($\geq$ 2700 m BTB), the probability of exceeding critical pressure was largest for an intermediate number of fractures (i.e. 1000 or 2000 fractures). Similarly, Fig. (b) shows the probability of seismicity and EOF as a function of depth and number of fractures (i.e. $P(d_{seismicity} \geq d)$ vs d and $P(d_{EOF} \geq d)$ versus d). The probability of seismicity and EOF both increased with increasing number of fractures at shallow depths. At depths $\geq$ 2100 m BTB, the probability of seismicity and EOF was highest for an intermediate number of fractures (i.e. 1000 fractures). The figures also have dashed lines indicating 2 km BTB, where the fault is centered, and dotted lines indicating the top and bottom of the fault.

Fig. 9(a), the probability of exceeding critical pressure was unaffected by the choice of the hydraulic diffusivity relationship at depths shallower than 1300 m. At greater depths, the "Bandis" scenario resulted in a modest increase in the probability of critical pressure, when compared to the "Constant" scenario. The "MC-Bandis" scenario resulted in a considerably larger probability of critical pressure, especially at $d \geq 3300$ m, compared to the "Constant" scenario. Fig. 9(b) shows the probability of seismicity as a function of depth and hydraulic diffusivity constitutive relationship. The probability of seismicity was larger for the "MC-Bandis" scenario than for the "Bandis" scenario, especially at the deeper parts of the fault ($d \geq 2500$ m).

Why does the MC permeability enhancement seem to be important while the Bandis effect is less important? Firstly, MC failure enhances permeability, which increases the hydraulic diffusivity, whereas Bandis dilation increases the permeability and the porosity, which have competing effects on the hydraulic diffusivity (Eq. 1). Secondly, based on the Bandis model, fractures are forced almost entirely shut at the depths and lithostatic stresses commonly seen near IIS. As fractures are forced closed, their stiffness increases and asymptotes to infinity so that the stiffness of the fracture/matrix system approaches that of the matrix rock. Therefore, in the context of IIS, the fractures are unlikely to open very much as pore pressure is increased. Nevertheless, the Bandis dilation could prove to be more important in geologic settings where the effective normal stress is less compressive and fractures can open and close to a greater degree. It is clear that the MC permeability enhancement is an important factor in propagating critical pressure to ≥ 2 km.

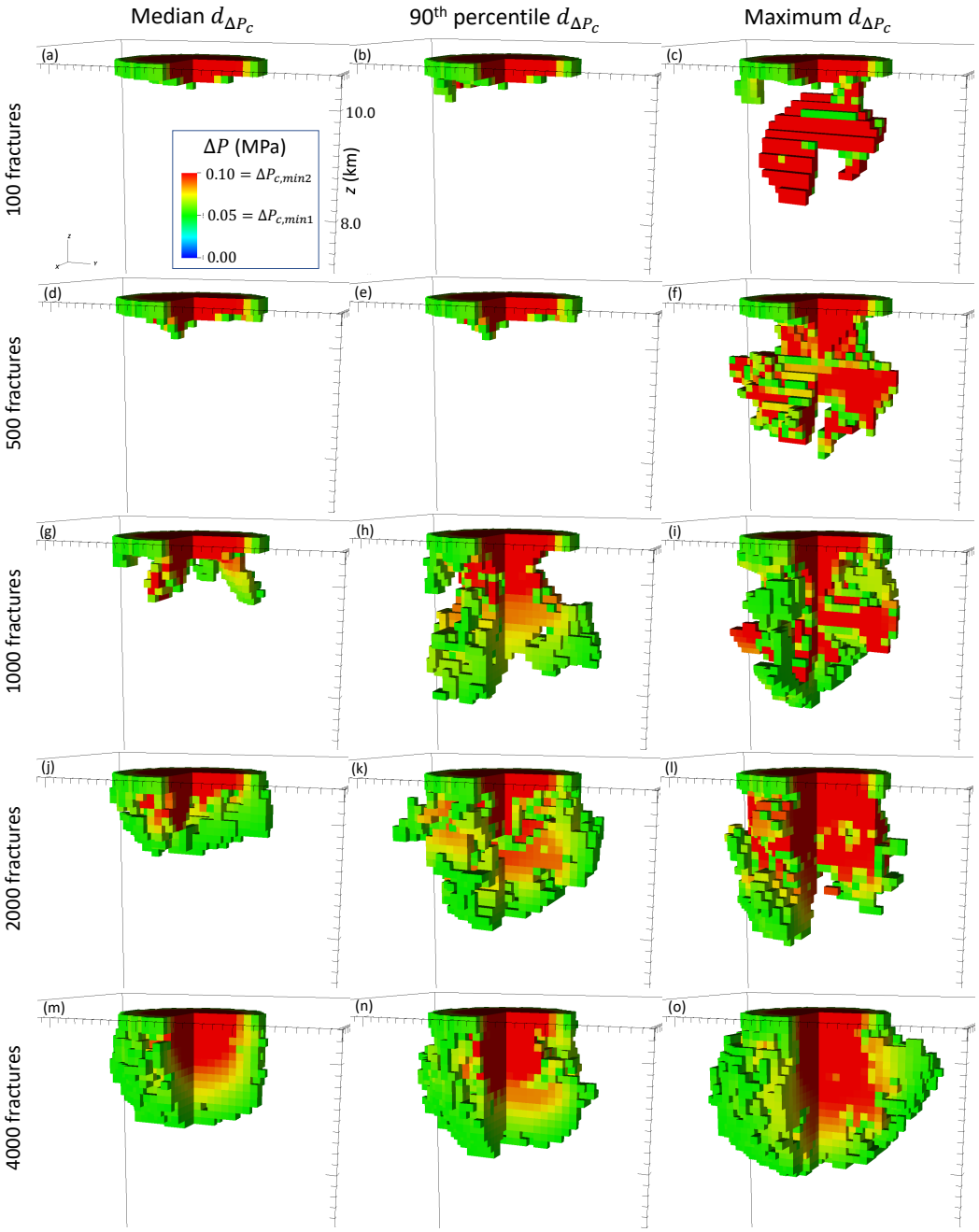

Figure 7. The spatial distribution of $\Delta P_{c,min}$ for the fracture-density sensitivity analysis. Regions where $\Delta P < \Delta P_{c,min1} = 0.05$ MPa are not shown because they cannot experience seismicity, and regions where $\Delta P > \Delta P_{c,min2} = 0.1$ MPa are colored red. The fracture density increases by rows going down. The subfigures in the left column (i.e. (a), (d), (g), (j), and (m)) show the pressure profiles for the realization with the median $d_{\Delta P_c}$. The subfigures in the center column (i.e. (b), (e), (h), (k), and (n)) show the pressure profile for the realization with the ninetieth percentile of $d_{\Delta P_c}$. The subfigures in the right column (i.e. (c), (f), (i), (l), and (o)) show the pressure profile for the realization with the maximum $d_{\Delta P_c}$. The median $d_{\Delta P_c}$ increases with the number of fractures, but the ninetieth percentile and maximum $d_{\Delta P_c}$ both exhibit a non-monotonic relationship and are largest at an intermediate fracture density (1000 fractures). Also note that flow becomes pseudo-spherical as fracture density increases.

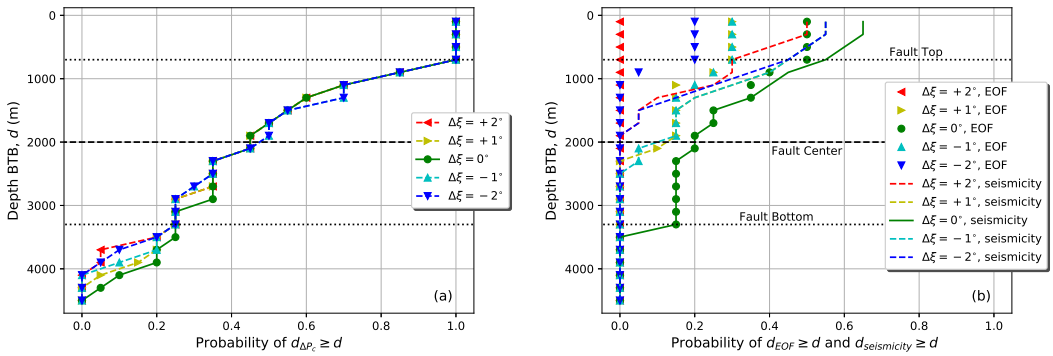

Figure 8. Fig. (a) shows the probability of exceeding critical pressure ($\geq \Delta P_{c,min1} = 0.05$ MPa) as a function of depth and the orientation of the deterministically-located fault, which is expressed by plotting $P(d_{\Delta P_c} \geq d)$ versus d. In the legend, $\Delta\xi$ is the angle by which the fault deviates from its optimal orientation, so that $\Delta\xi = -2^{\circ}$ corresponds to a fault that is two degrees more vertical than an optimal-orientation. At some shallow depths (e.g. 1300 m BTB and 1900 m BTB), the vertically-deviated faults slightly increased the probability of exceeding critical pressure. At greater depths (e.g. 2700–2900 m BTB and $\geq$ 3500 m), the optimally-oriented fault had the highest probability of exceeding critical pressure because it was more likely to experience enhanced permeability due to MC failure. Fig. (b) shows the probability of seismicity and EOF as a function of depth and the orientation of the deterministically-located fault (i.e. $P(d_{seismicity} \geq d)$ versus d and $P(d_{EOF} \geq d)$ versus d). The probability of seismicity is greatest at shallow depths. The probability of seismicity decreased with depth more rapidly for realizations with faults that were deviated from the optimal orientation. In the simulations with fault deviation of $\pm 2^{\circ}$, there was a zero percent chance of seismicity at $d \geq 1900$ m BTB, whereas the simulations with an optimally-oriented fault had a 15% chance of seismicity even much deeper at $d = 3300$ m BTB. The probability of EOF was affected even more dramatically by fault orientation than the probability of seismicity. d_{EOF} reached the bottom of the fault in 15% of realizations with an optimally-oriented fault and in 0% of realizations with any deviation from optimal orientation. EOFs never occurred on a fault with an angle of $+2^{\circ}$. The figures also have dashed lines indicating 2 km BTB, where the fault is centered, and dotted lines indicating the depths of the top and bottom of the fault.

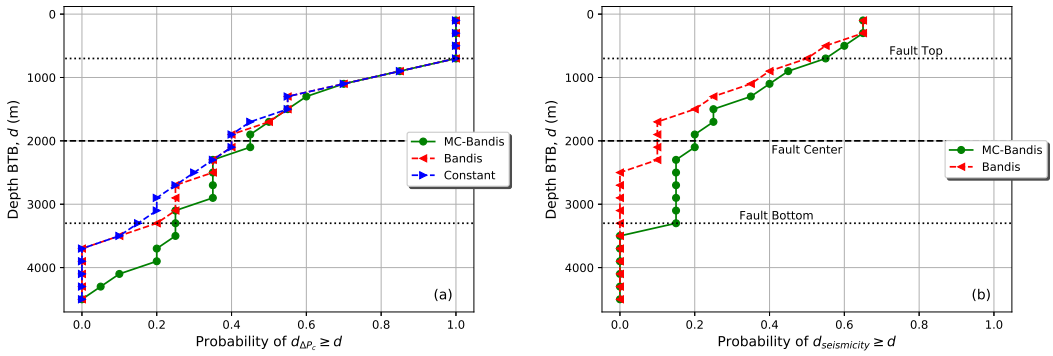

Figure 9. Fig. (a) shows the probability of exceeding critical pressure ($\geq \Delta P_{c,min1} = 0.05$ MPa) as a function of depth and the hydraulic diffusivity constitutive relationship that was used in the fractures/faults, which is expressed by plotting $P(d_{\Delta P_c} \geq d)$ versus d. In "MC-Bandis" the hydraulic diffusivity of fractures/faults is altered by both MC shear failure and the opening of fractures in the normal direction according to the Bandis relationship (see Eq. 8), in "Bandis" the hydraulic diffusivity of fractures/faults is altered by the Bandis relationship but not MC, and in "Constant" the hydraulic diffusivity is constant in time and matches the initial hydraulic diffusivity of the "MC-Bandis" and "Bandis" scenarios (see Table 4). Fig. (b) shows the probability of seismicity as a function of depth and the hydraulic diffusivity constitutive relationship (i.e. $P(d_{seismicity} \geq d)$ versus d). Seismicity was not calculated for the "Constant" scenario and EOF was not calculated for the "Bandis" scenario, so these data are not shown in the figure. The figures have dashed lines indicating 2 km BTB, where the fault is centered, and dotted lines indicating the depths of the top and bottom of the fault.

6 Discussion and Conclusions

The rise in IIS in the central USA has been attributed to the disposal of wastewater. The most common explanation for IIS involves diffusion of elevated pore pressures from disposal wells to critically-stressed faults, thereby destabilizing the faults and leading to MC failure and seismicity. To drive this destabilizing mechanism, elevated pressures must diffuse through low-permeability, fractured/faulted basement rock to seismogenic depths ($\geq$ 2 km BTB) where the basement is most-critically stressed (Vilarrasa & Carrera, 2015) and the majority of IIS has been observed in the central U.S. (Nakai et al., 2017; W. L. Yeck et al., 2016; Schoenball & Ellsworth, 2017). It is clear that fractures and faults are important both hydraulically, as preferential flow pathways, and mechanically, as the locations that host seismicity (Shah & Keller, 2017; National Research Council, 2013). Despite the importance of fractures and faults, many numerical models of IIS have employed an EPM-TP approach, which smooths out the hydraulic influence of fractures and faults and neglects mechanical considerations in the earthquake-triggering mechanism (Keranen et al., 2014; Brown et al., 2017; Langenbruch et al., 2018; Shirzaei et al., 2016; Pollyea et al., 2019; Nakai et al., 2017; Hearn et al., 2018; Zhang et al., 2013; Ogwari et al., 2018; Schoenball et al., 2018). The EPM-TP approach does not address key questions such as: (1) how fluid pressure diffuses through low permeability basement rock to seismogenic depths, (2) how important the deformation-induced changes in hydraulic diffusivity are to bringing pressure to depth, and (3) why IIS is rather uncommon given the large number of disposal wells (Ellsworth, 2013; Nicholson & Wesson, 1992; U.S. EPA, 2018) and the prevalence of critically-stressed conditions in basement formations (Townend & Zoback, 2000).

To address the above questions, we developed a DFNM-MC numerical model to simulate pressure diffusion in the context of IIS. It builds upon the approach of previously developed simulators that represent fracture and matrix flow, coupled hydro-mechanical processes, deformation-induced changes in the hydraulic diffusivity, and MC failure (Jin & Zoback, 2018, 2017; Jha & Juanes, 2014; Ucar et al., 2018; Rinaldi et al., 2014; Kelkar et al., 2014). The DFNM-MC model is novel because of its capability to simulate thousands of deformable fractures and faults within large, 3D domains ($\sim$10 x 10 x 10 km), which has not previously been done in the context of IIS. This is computationally possible because the DFNM-MC approach leverages parallelization and simplified partial coupling between geomechanics and fluid flow, based on the assumption of a time-invariant stress field. The DFNM-MC approach can be used for other subsurface applications where flow occurs in matrix rock and deformable fractures (e.g. hydrocarbon production from hydraulically fractured reservoirs).

To consistently model scenarios relevant to IIS, we must consistently represent the hydraulic diffusivity of basement rock. The hydraulic diffusivity of fractured basement rock at the reservoir to basin scale is $c_{bulk} = 10^{-6}$–10^{-3} m^2/s (Table 1). This is based on the accepted values for porosity, permeability, water properties, and the compressibility of fractured rock (Sec. 2.2) (Freeze & Cherry, 1979; Manning & Ingebritsen, 1999). To be consistent, EPM-TP models should employ c_{bulk}, but they instead tend to use unrealistically large values in order to achieve rapid pressure propagation to locations of seismicity. On the other hand, our DFNM-MC approach employs realistic hydraulic parameters (permeability and compressibility). Rapid pressure propagation to greater depths is facilitated by connected fractures that form preferential flow pathways with relatively low leakoff rates into the surrounding matrix. We know the hydraulic parameters are realistic for several reasons. Firstly the unfractured region of the basement employs c_{core}, and the fractured regions of the model employ diffusivities consistent with experimentally measured properties of fractures (Bandis et al., 1983; Murphy et al., 2004). Secondly, the equivalent hydraulic diffusivity that was derived from the DFNM model for scenario EPM1 in Sec. 5.1 is equal to c_{bulk}, as it should be. Finally, the DFNM-MC model brings $\Delta P_{c,min}$ to seismogenic depths in a time frame that is consistent with field ob-

servations. For example, in Sec. 5.1, $\Delta P_{c,min}$ diffuses to 2150 m BTB after three years of injection.

The fracture diffusivity ($c_{fracture}$) in our models is much greater than the seismogenic diffusivity (c_{sT}) reported by Talwani et al. (2007), and also greater than the hydraulic diffusivity that we would infer based on the speed of $\Delta P_{c,min}$ diffusion in our model simulations. Clearly, the effective hydraulic diffusivity inferred from pressure propagation in a fracture-matrix system is smaller than $c_{fracture}$, due to leakoff and the tortuosity of the fracture network. Questions may be raised about the precise meaning of the seismogenic diffusivity – it is not clear whether it is equal to the equivalent hydraulic diffusivity or a much larger quantity, reflecting the influence of preferential flow pathways within fractured rock. But our simulations suggest that the seismogenic diffusivity falls somewhere in between c_{bulk} and $c_{fracture}$. Our results also show that propagation of seismic events is maximized at an intermediate fracture density (Sec. 5.2.1). Since an intermediate fracture density corresponds to an intermediate effective hydraulic diffusivity, this result provides a plausible explanation for why seismicity only occurs over a narrow intermediate range of (seismogenic) diffusivity values, as pointed out by Talwani et al. (2007). The seismogenic diffusivity depends on the connectivity of fractures in selectively propagating pressure perturbations ahead of a "mean" pressure front. It also depends on the contrast between the fracture and matrix hydraulic diffusivity (Haagenson et al., 2018a, 2018b), with higher leakoff rates reducing the distance between the most distant pressure front and the mean pressure front. The seismogenic diffusivity should not be interpreted as the hydraulic diffusivity until we have a better understanding of what it represents.

The DFNM-MC approach is a clear improvement over the EPM-TP approach for simulating reservoir- to basin-scale IIS. Comparison of the DFNM-MC approach with the three EPM scenarios (Sec. 5.1), offers insight into why previous EPM-TP studies have needed to employ unrealistically-large values of hydraulic diffusivity. In scenario EPM1, which is based on the equivalent permeability corresponding to the DFNM-MC simulations and a compressibility consistent with a value for jointed crystalline rock (Freeze & Cherry, 1979), critical pressure does not diffuse to seismogenic depths. Scenario EPM2 utilized the same parameters as Brown et al. (2017), including an unrealistically small value of compressibility and a corresponding large value of hydraulic diffusivity, thus producing critical pressure propagation to seismogenic depths. EPM3, on the other hand, employed the same permeability as Brown et al. (2017) but used a more realistic value of matrix compressibility, and it did not result in pressures reaching seismogenic depths. The problem with many of the EPM-TP studies has been in their assignment of the porous medium compressibility, which should be larger than the compressibility of intact crystalline rock due to the presence of fractures (Freeze & Cherry, 1979). The overall rationale for employing EPM-TP studies to infer the mechanisms driving IIS is somewhat tenuous – in many of these studies, the hydraulic diffusivity (or equivalently the hydraulic conductivity) was calibrated to reproduce elevated pressure at the earthquake hypocenters (Keranen et al., 2014; Brown et al., 2017). The same studies then concluded that pressure diffusion was a plausible causative mechanism, despite the unrealistically large calibrated values for hydraulic diffusivity. Another problem with the EPM-TP approach is that it does not define the locations of fractures and it cannot resolve the actual ΔP_c (which is a function of fracture/fault orientation, the initial local stress and pressure, and fracture properties) that is required to cause seismicity. The EPM-TP approach simply results in a region where $\Delta P > TP$ where seismicity may occur. Since the EPM approach gives smooth pressure profiles, there are large, laterally-extensive regions that are critically-pressured. This would suggest that IIS should be much more prevalent than it actually is (i.e. the EPM-TP approach would lead to many false positives of IIS if used predictively). In contrast, the DFNM-MC approach supplies information about the location, ΔP_c, and time of MC failure, which are unique for each fracture/fault.

Our results from the DFNM-MC sensitivity analysis (Sec. 5.2) show that pressure diffusion to seismogenic depths and earthquake triggering are more nuanced and less likely than the EPM-TP models have shown. For pressure propagation to the relevant seismogenic depths, the fracture density generally needs to be an optimal, intermediate value (Sec. 5.2.1). Too few fractures generally result in insufficient hydraulic connectivity, while too many fractures result in flow paths that compete for flow so that pressure diffusion is also limited in depth. Even with an optimal, intermediate fracture density, many DFN realizations do not provide connected hydraulic pathways to depth. In addition, our results show that the deformation-induced changes in hydraulic conductivity (especially from shear failure in the shallow basement) play an important role in allowing pressure to propagate to $\geq$ 2 km BTB (Sec. 5.2.3). The normal deformation described by the Bandis et al. (1983) relationship is only marginally important in our simulations because fractures are held tightly closed at the effective stresses found deep in the basement. But this effect could prove more important in other applications, such as production of O&G, heat for geothermal energy, or potable water from fractured reservoirs, in which the confining stresses are smaller and pressure changes will alter the fracture aperture more easily. Previous studies have shown the importance of deformation-induced permeability changes (e.g. Ucar et al. (2018)), but not within the context of IIS with thousands of fractures. Previous studies have also pointed out that the presence of an underlying confining layer can preclude pressure diffusion to seismogenic depths (Zhang et al., 2013). Furthermore, the orientation of fractures and faults is important in dictating the probability of IIS; it is possible to have pressure diffuse to depths $\geq$ 2 km BTB with only very limited seismicity. In our simulations, the depth of IIS always lags behind the depth of $\Delta P_{c,min}$, sometimes by a substantial distance, because deviations from the optimal orientation increase ΔP_c to values larger than $\Delta P_{c,min}$. Changes in the orientation of the fault by as small as $\Delta\xi = \pm 2^{\circ}$ (corresponding to 0.13 MPa change in ΔP_c) are enough to entirely preclude seismicity on a major fault (EOF) in our sensitivity analysis (Sec. 5.2.2). Any one of the factors discussed in this paragraph (fracture network density, fracture network connectivity, lack of enhanced hydraulic diffusivity in shallower fractures/faults, an underlying confining layer, and the orientation of faults at $\geq$ 2 km BTB) may be enough to prevent IIS by either precluding pressure diffusion to depth or by raising the required critical pressure for MC failure. This offers a viable explanation for why only a small fraction of Class II disposal wells are associated with IIS in the USA.

We have several recommendations for future study and mitigation of IIS. First, data about fractures and faults in basement formations should be collected and shared. In particular, more work should be done to understand the fracture statistics of basement rock. This work could help to establish the real-world fracture statistics that correspond to the intermediate fracture density case in our sensitivity analysis (Sec. 5.2.1), and it could also be compared to the types of basement rock where IIS is most likely, along the lines of Shah and Keller's (2017) findings. Injection near basement formations with an intermediate fracture density and/or unfavorable basement rock type, which can promote deep pressure propagation, could be avoided. Furthermore, we suggest that publicly-available basement fault databases should be augmented to include faults identified in proprietary data, along with their orientation relative to the local stress field. Open sharing of such data would help both industry and regulators avoid wastewater disposal into areas where pressure could diffuse into large, optimally-oriented basement faults. Many of the data discussed in this paragraph is also useful for site-specific DFNM-MC simulations, which require: (i) the location, orientation, and MC parameters for all major faults; (ii) the Bandis parameters and location, size, and orientation statistics for fractures; (iii) the in situ stress state and initial pressure; and (iv) hydraulic properties of the disposal formation.

The scientific community needs to move past EPM-TP models when trying to understand IIS. The ideal modeling tool to understand IIS would include full hydro-mechanical coupling with a fracture and matrix approach that would allow for multiple MC failure

events at the same location, update the hydraulic diffusivity as a function of fracture deformation, and include propagation of seismic waves and evaluation of the Coulomb stress change after MC failure. To our knowledge, this type of tool does not exist, and even simulators that do not propagate seismic waves are generally limited to 2D (Jin & Zoback, 2018, 2017) or a single fault (Jha & Juanes, 2014; Rinaldi et al., 2014; Kelkar et al., 2014) due to computational cost. For computational expediency, it may be possible to implement fracture and matrix simulators wherein the mechanical and hydrologic equations are fully coupled but the mechanical solution is not updated in every time step of the hydrologic calculation, but these have not been presented in the literature to our knowledge. Therefore, our partially-coupled DFNM-MC approach is especially attractive, because it can simulate large spatial scales with many fractures and faults. The DFNM-MC approach can contribute to probabilistic assessment of the risks of induced seismicity based on the datasets described in the previous paragraph. As demonstrated in Sec. 5.2, the DFNM-MC approach can be combined with Monte-Carlo simulations on multiple realizations of fracture networks across which fracture and fault locations, orientations, and properties are sampled from their respective probability density functions. The partially coupled nature and the parallelization of the DFNM-MC approach renders it computationally tractable for such probabilistic assessments. While forecasting IIS is still extremely difficult, a DFNM-MC model with all the relevant parameters could, in principle, offer a screening framework for forecasting before injection begins and/or during injection as part of an adaptive traffic light system (Wiemer et al., 2015; Király-Proag et al., 2016). One drawback of the partially-coupled DFNM-MC model is that it cannot evaluate poroelastic stress changes, earthquake-earthquake interactions, or allow for multiple failure events. Simulators that can evaluate these phenomena are computationally expensive, so the partially-coupled DFNM-MC approach could be used in a screening step to identify the most critical scenarios for further investigation with other, computationally-expensive simulators.

Acknowledgments

We thank Los Alamos National Laboratory Center for Space and Earth Science, the National Science Foundation Hazards SEES project EAR 1520846, and the University of Colorado Dissertation Completion Fellowship for financial support. We also thank Jeffrey Hyman and the rest of the dfnWorks team for helpful discussions about our algorithm that generates and maps fractures to the PFLOTRAN grid. All of the data presented in this study are from simulation results and are presented in figures and tables within the text and the supporting information and are also available at http://hdl.handle.net/20.500.11850/395361 under the DOI:10.3929/ethz-b-000395361. There are no conflicts of interest to report.

References

Bandis, S., Lumsden, A., & Barton, N. (1983). Fundamentals of rock joint deformation. *International journal of rock mechanics and mining sciences*, *20*(6), 249–268.

Birdsell, D. T. (2018). *An investigation of subsurface fluid injections related to oil and gas development: Modeling hydraulic fracturing fluid migration and induced seismicity.* (PhD dissertation (University of Colorado, Boulder))

Birdsell, D. T., Karra, S., & Rajaram, H. (2018). On the representation of the porosity-pressure relationship in general subsurface flow codes. *Water Resources Research*, *54*(2), 1382–1388.

Birdsell, D. T., Rajaram, H., Dempsey, D., & Viswanathan, H. S. (2015). Hydraulic fracturing fluid migration in the subsurface: A review and expanded modeling results. *Water Resources Research*, *51*(9), 7159–7188.

Birdsell, D. T., Rajaram, H., & Karra, S. (2018). Code development for modeling induced seismicity with flow and mechanics using a discrete fracture network

and matrix formulation with evolving hydraulic diffusivity. In *2nd international discrete fracture network engineering conference.* Seattle, WA. (DFNE 18-565.)

Bower, K., & Zyvoloski, G. (1997). A numerical model for thermo-hydro-mechanical coupling in fractured rock. *International Journal of Rock Mechanics and Mining Sciences*, *34*(8), 1201–1211.

Brown, M. R., & Ge, S. (2018). Small earthquakes matter in injection-induced seismicity. *Geophysical Research Letters*, *45*(11), 5445–5453.

Brown, M. R., Ge, S., Sheehan, A. F., & Nakai, J. S. (2017). Evaluating the effectiveness of induced seismicity mitigation: Numerical modeling of wastewater injection near Greeley, Colorado. *Journal of Geophysical Research: Solid Earth*, *122*(8), 6569–6582.

Chang, K., & Segall, P. (2016). Injection-induced seismicity on basement faults including poroelastic stressing. *Journal of Geophysical Research: Solid Earth*, *121*(4), 2708–2726.

Chaudhuri, A., Rajaram, H., & Viswanathan, H. (2013). Early-stage hypogene karstification in a mountain hydrologic system: A coupled thermohydrochemical model incorporating buoyant convection. *Water Resources Research*, *49*(9), 5880–5899.

De Marsily, G. (1986). *Quantitative hydrogeology: groundwater hydrology for engineers.* Orlando, FL: Academic Press, Inc.

Dempsey, D., & Riffault, J. (2019). Response of induced seismicity to injection rate reduction: Models of delay, decay, quiescence, recovery, and Oklahoma. *Water Resources Research*, *55*(1), 656–681.

Einstein, H. H., & Dershowitz, W. S. (1990). Tensile and shear fracturing in predominantly compressive stress fields—a review. *Engineering Geology*, *29*(2), 149–172.

Ellsworth, W. L. (2013). Injection-induced earthquakes. *Science*, *341*(6142), 1225942.

Evans, K., Moriya, H., Niitsuma, H., Jones, R., Phillips, W., Genter, A., ... Baria, R. (2005). Microseismicity and permeability enhancement of hydrogeologic structures during massive fluid injections into granite at 3 km depth at the Soultz HDR site. *Geophysical Journal International*, *160*(1), 388–412.

Freeze, R. A., & Cherry, J. A. (1979). *Groundwater, 604 pp.* Englewood Cliffs, NJ: Prentice-Hall.

Goebel, T., Weingarten, M., Chen, X., Haffener, J., & Brodsky, E. (2017). The 2016 Mw 5.1 Fairview, Oklahoma earthquakes: Evidence for long-range poroelastic triggering at >40 km from fluid disposal wells. *Earth and Planetary Science Letters*, *472*, 50–61.

Haagenson, R., Rajaram, H., Karra, S., & Allen, J. (2018a). Modeling nonlinear diffusion in fractured rock with deformable fractures and applications to injection induced seismicity. In *52nd us rock mechanics/geomechanics symposium and discrete fracture network engineering conference.* (DFNE 18-426)

Haagenson, R., Rajaram, H., Karra, S., & Allen, J. (2018b, May). *Modeling nonlinear diffusion in fractured rock. With deformable fractures and applications to injection induced seismicity.* (Presentation at the InterPore 10th Annual Meeting and Jubilee. New Orleans, LA)

Hammond, G. E., Lichtner, P. C., & Mills, R. T. (2014). Evaluating the performance of parallel subsurface simulators: An illustrative example with PFLOTRAN. *Water Resources Research*, *50*, 208-228. doi: 10.1002/2012WR013483

Healy, J., Rubey, W., Griggs, D., & Raleigh, C. (1968). The Denver Earthquakes. *Science*, *161*(3848), 1301–1310.

Hearn, E. H., Koltermann, C., & Rubinstein, J. L. (2018). Numerical models of pore pressure and stress changes along basement faults due to wastewater injection: Applications to the 2014 Milan, Kansas earthquake. *Geochemistry, Geophysics,*

Geosystems, *19*(4), 1178–1198.

Hyman, J., Painter, S. L., Viswanathan, H., Makedonska, N., & Karra, S. (2015). Influence of injection mode on transport properties in kilometer-scale three-dimensional discrete fracture networks. *Water Resources Research*, *51*(9), 7289–7308.

Jha, B., & Juanes, R. (2014). Coupled multiphase flow and poromechanics: A computational model of pore pressure effects on fault slip and earthquake triggering. *Water Resources Research*, *50*(5), 3776–3808.

Jin, L., & Zoback, M. (2017). Fully coupled nonlinear fluid flow and poroelasticity in arbitrarily fractured porous media: A hybrid-dimensional computational model. *Journal of Geophysical Research: Solid Earth*, *122*(10), 7626–7658.

Jin, L., & Zoback, M. (2018). Modeling induced seismicity: Inter-seismic quasi-static triggering in a discretely fractured poroelastic medium. In *2nd international discrete fracture network engineering conference.*

Kelkar, S., Lewis, K., Karra, S., Zyvoloski, G., Rapaka, S., Viswanathan, H., ... Pawar, R. (2014). A simulator for modeling coupled thermo-hydro-mechanical processes in subsurface geological media. *International Journal of Rock Mechanics and Mining Sciences*, *70*, 569–580.

Kelkar, S., Zyvoloski, G., Rapaka, S., & Yoshioka, K. (2011). *Modeling shear failure and permeability enhancement due to coupled thermal-hydrological-mechanical processes in enhanced geothermal reservoirs* (Tech. Rep. No. LA-UR-11-10610). Los Alamos, NM: Los Alamos National Laboratory.

Keranen, K. M., Weingarten, M., Abers, G. A., Bekins, B. A., & Ge, S. (2014). Sharp increase in central Oklahoma seismicity since 2008 induced by massive wastewater injection. *Science*, *345*(6195), 448–451.

Király-Proag, E., Zechar, J. D., Gischig, V., Wiemer, S., Karvounis, D., & Doetsch, J. (2016). Validating induced seismicity forecast models—induced seismicity test bench. *Journal of Geophysical Research: Solid Earth*, *121*(8), 6009–6029.

Lang, P. S., Paluszny, A., Nejati, M., & Zimmerman, R. W. (2018). Relationship between the orientation of maximum permeability and intermediate principal stress in fractured rocks. *Water Resources Research*, *54*(11), 8734–8755.

Langenbruch, C., Weingarten, M., & Zoback, M. D. (2018). Physics-based forecasting of man-made earthquake hazards in oklahoma and kansas. *Nature communications*, *9*(1), 3946.

Langenbruch, C., & Zoback, M. D. (2016). How will induced seismicity in Oklahoma respond to decreased saltwater injection rates? *Science advances*, *2*(11), e1601542.

Lichtner, P. C., Hammond, G. E., Lu, C., Karra, S., Bisht, G., Andre, B., ... Frederick, J. M. (2019a). *PFLOTRAN user manual* (Tech. Rep.). (http://documentation.pflotran.org)

Lichtner, P. C., Hammond, G. E., Lu, C., Karra, S., Bisht, G., Andre, B., ... Frederick, J. M. (2019b). *PFLOTRAN Web page.* (http://www.pflotran.org)

Mallikamas, W., & Rajaram, H. (2005). On the anisotropy of the aperture correlation and effective transmissivity in fractures generated by sliding between identical self-affine surfaces. *Geophysical research letters*, *32*(11).

Manning, C., & Ingebritsen, S. (1999). Permeability of the continental crust: Implications of geothermal data and metamorphic systems. *Reviews of Geophysics*, *37*(1), 127–150.

Morrow, C., & Lockner, D. (1997). Permeability and porosity of the Illinois UPH 3 drillhole granite and a comparison with other deep drillhole rocks. *Journal of Geophysical Research: Solid Earth*, *102*(B2), 3067–3075.

Murphy, H., Huang, C., Dash, Z., Zyvoloski, G., & White, A. (2004). Semianalytical solutions for fluid flow in rock joints with pressure-dependent openings. *Water resources research*, *40*(12).

Nakai, J., Weingarten, M., Sheehan, A., Bilek, S., & Ge, S. (2017). A possible

causative mechanism of Raton Basin, New Mexico and Colorado earthquakes using recent seismicity patterns and pore pressure modeling. *Journal of Geophysical Research: Solid Earth*, *122*(10), 8051–8065.

National Research Council. (2013). *Induced seismicity potential in energy technologies*. Washington, D.C.: National Academies Press. (13: 978-0-309-25367-3)

Nicholson, C., & Wesson, R. L. (1992). Triggered earthquakes and deep well activities. *Pure and applied Geophysics*, *139*(3-4), 561–578.

Norbeck, J., & Rubinstein, J. L. (2018). Hydromechanical earthquake nucleation model forecasts onset, peak, and falling rates of induced seismicity in Oklahoma and Kansas. *Geophysical Research Letters*, *45*(7), 2963–2975.

Ogwari, P. O., DeShon, H. R., & Hornbach, M. J. (2018). The Dallas-Fort Worth airport earthquake sequence: Seismicity beyond injection period. *Journal of Geophysical Research: Solid Earth*, *123*(1), 553–563.

Pandey, S., Chaudhuri, A., & Kelkar, S. (2017). A coupled thermo-hydro-mechanical modeling of fracture aperture alteration and reservoir deformation during heat extraction from a geothermal reservoir. *Geothermics*, *65*, 17–31.

Peterie, S. L., Miller, R. D., Intfen, J. W., & Gonzales, J. B. (2018). Earthquakes in Kansas induced by extremely far-field pressure diffusion. *Geophysical Research Letters*, *45*(3), 1395–1401.

Pollyea, R. M., Chapman, M. C., Jayne, R. S., & Wu, H. (2019). High density oilfield wastewater disposal causes deeper, stronger, and more persistent earthquakes. *Nature communications*, *10*(1), 3077.

Riffault, J., Dempsey, D., Karra, S., & Archer, R. (2018). Microseismicity cloud can be substantially larger than the associated stimulated fracture volume: the case of the paralana enhanced geothermal system. *Journal of Geophysical Research: Solid Earth*, *123*(8), 6845–6870.

Rinaldi, A. P., Jeanne, P., Rutqvist, J., Cappa, F., & Guglielmi, Y. (2014). Effects of fault-zone architecture on earthquake magnitude and gas leakage related to CO_2 injection in a multi-layered sedimentary system. *Greenhouse Gases: Science and Technology*, *4*(1), 99–120.

Rinaldi, A. P., & Nespoli, M. (2017). Tough2-seed: A coupled fluid flow and mechanical-stochastic approach to model injection-induced seismicity. *Computers & Geosciences*, *108*, 86–97.

Rutqvist, J., Birkholzer, J., Cappa, F., & Tsang, C.-F. (2007). Estimating maximum sustainable injection pressure during geological sequestration of CO_2 using coupled fluid flow and geomechanical fault-slip analysis. *Energy Conversion and Management*, *48*(6), 1798–1807.

Schoenball, M., & Ellsworth, W. L. (2017). Waveform-relocated earthquake catalog for Oklahoma and Southern Kansas illuminates the regional fault network. *Seismological Research Letters*, *88*(5), 1252–1258.

Schoenball, M., Walsh, F. R., Weingarten, M., & Ellsworth, W. L. (2018). How faults wake up: the Guthrie-Langston, Oklahoma earthquakes. *The Leading Edge*, *37*(2), 100–106.

Shah, A. K., & Keller, G. R. (2017). Geologic influence on induced seismicity: Constraints from potential field data in Oklahoma. *Geophysical Research Letters*, *44*(1), 152–161.

Shapiro, S., & Dinske, C. (2009). Fluid-induced seismicity: Pressure diffusion and hydraulic fracturing. *Geophysical Prospecting*, *57*(2), 301–310.

Shirzaei, M., Ellsworth, W. L., Tiampo, K. F., González, P. J., & Manga, M. (2016). Surface uplift and time-dependent seismic hazard due to fluid injection in eastern Texas. *Science*, *353*(6306), 1416–1419.

SKB. (2011, March). *Long-term safety for the final repository for spent nuclear fuel at Forsmark* (Tech. Rep. No. SKB TR-11-01). Stockholm: AB, Svensk Kärnbränslehantering.

Talwani, P., Chen, L., & Gahalaut, K. (2007). Seismogenic permeability, ks. *Journal*

of Geophysical Research: Solid Earth, *112*(B7).

Townend, J., & Zoback, M. D. (2000). How faulting keeps the crust strong. *Geology*, *28*(5), 399–402.

Ucar, E., Berre, I., & Keilegavlen, E. (2018). Three-dimensional numerical modeling of shear stimulation of fractured reservoirs. *Journal of Geophysical Research: Solid Earth*, *123*(5), 3891–3908.

U.S. EPA. (2018). *Fiscal year 2018 underground injection controll (UIC) injection well inventory.* `https://www.epa.gov/uic/uic-injection-well-inventory`. U.S. Environmental Protection Agency. (Accessed: July 30, 2019)

Vilarrasa, V., & Carrera, J. (2015). Geologic carbon storage is unlikely to trigger large earthquakes and reactivate faults through which CO_2 could leak. *Proceedings of the National Academy of Sciences*, *112*(19), 5938–5943.

Weingarten, M., Ge, S., Godt, J. W., Bekins, B. A., & Rubinstein, J. L. (2015). High-rate injection is associated with the increase in us mid-continent seismicity. *Science*, *348*(6241), 1336–1340.

Wiemer, S., Kraft, T., & Landtwing, D. (2015). Ch 6.2: Seismic risk. In S. Hirschberg, S. Wiemer, & P. Burgherr (Eds.), *Energy from the earth: Deep geothermal as a resource for the future?* (pp. 263–295). doi: 10.3218/3655-8

Witherspoon, P. A., Wang, J. S., Iwai, K., & Gale, J. E. (1980). Validity of cubic law for fluid flow in a deformable rock fracture. *Water resources research*, *16*(6), 1016–1024.

Wood, A. T. (1994). Simulation of the von Mises Fisher distribution. *Communications in statistics-simulation and computation*, *23*(1), 157–164.

Yeck, W., Weingarten, M., Benz, H. M., McNamara, D. E., Bergman, E., Herrmann, R., ... Earle, P. (2016). Far-field pressurization likely caused one of the largest injection induced earthquakes by reactivating a large preexisting basement fault structure. *Geophysical Research Letters*, *43*(19), 1-10.

Yeck, W. L., Sheehan, A., Benz, H. M., Weingarten, M., & Nakai, J. (2016). Rapid response, monitoring, and mitigation of induced seismicity near Greeley, Colorado. *Seismological Research Letters*, *87*(4), 837–847.

Zhang, Y., Person, M., Rupp, J., Ellett, K., Celia, M. A., Gable, C. W., ... others (2013). Hydrogeologic controls on induced seismicity in crystalline basement rocks due to fluid injection into basal reservoirs. *Groundwater*, *51*(4), 525–538.

Zimmerman, R. W., & Bodvarsson, G. S. (1996). Hydraulic conductivity of rock fractures. *Transport in porous media*, *23*(1), 1–30.

Zoback, M. D. (2010). *Reservoir geomechanics.* United Kingdom: Cambridge University Press.